solids

MDPI

Article

Pristine and Reassembled Nanosheets of Layered Perovskite-like Titanates $HLnTiO_4$ and $H_2Ln_2Ti_3O_{10}$ (Ln = La, Nd) as Photocatalysts for Hydrogen Evolution

Sergei A. Kurnosenko , Oleg I. Silyukov *, Ivan A. Rodionov , Iana A. Minich and Irina A. Zvereva

Department of Chemical Thermodynamics and Kinetics, Institute of Chemistry, Saint Petersburg State University, 199034 Saint Petersburg, Russia; s.kurnosenko@spbu.ru (S.A.K.); i.rodionov@spbu.ru (I.A.R.); yana.minich@spbu.ru (I.A.M.); irina.zvereva@spbu.ru (I.A.Z.)

* Correspondence: oleg.silyukov@spbu.ru

Abstract: Layered Ruddlesden–Popper titanates $HLnTiO_4$ and $H_2Ln_2Ti_3O_{10}$ (Ln = La, Nd) have been exfoliated into nanosheets in aqueous tetrabutylammonium hydroxide and systematically investigated as hydrogen evolution photocatalysts. The nanosheets were tested both in as-prepared pristine form and after reassembly by two methods (simple filtration and precipitation by hydrochloric acid). The nanosheet-based samples demonstrated by up to 88 times greater photocatalytic performance in comparison with the bulk precursors and, after modification with a Pt cocatalyst, provided apparent quantum efficiency of hydrogen generation up to 14.2% in 1 mol.% aqueous methanol and 3.15% in pure water. It was established that the form in which the nanosheets are used strongly affects the hydrogen production efficiency: the latter typically decreases when moving from the pristine nanosheets to filtered ones and then to those restacked by hydrochloric acid, which is determined by the difference in their physical–chemical characteristics being influenced by the reassembly approach.

Keywords: photocatalysis; hydrogen; layered perovskite; exfoliation; nanosheets; reassembly

check for updates

Received: 19 January 2025
Revised: 12 February 2025
Accepted: 21 March 2025
Published: 2 April 2025

Citation: Kurnosenko, S.A.; Silyukov, O.I.; Rodionov, I.A.; Minich, I.A.; Zvereva, I.A. Pristine and Reassembled Nanosheets of Layered Perovskite-like Titanates $HLnTiO_4$ and $H_2Ln_2Ti_3O_{10}$ (Ln = La, Nd) as Photocatalysts for Hydrogen Evolution. *Solids* **2025**, *6*, 16. https://doi.org/10.3390/solids6020016

1. Introduction

In the context of depleting mineral reserves and tightening environmental legislation, heterogeneous photocatalysis is considered a powerful tool for renewable energy production as well as combating air and water pollution [1–3]. The continuous development of hydrogen evolution photocatalysts, initiated by the Fujishima and Honda's discovery of water photoelectrolysis [4], involves both the search for new, more efficient materials and applying advanced modifications to well-known ones [5–14], such as titanium dioxide TiO_2 [15–20]. Along with the splitting of pure water [21–30], photocatalytic reforming of bioalcohols, carbohydrates and other plant biomass derivatives is receiving more and more attention in recent studies because of the feasibility to obtain hydrogen from aqueous–organic media with much higher quantum yields [31–39].

An actively explored class of heterogeneous photocatalysts is represented by ion-exchangeable layered perovskite-like oxides—lamellar crystalline solids, whose structure consists of two-dimensional (2D) perovskite slabs, regularly interspersed with interlayer spaces populated by cations [40]. These oxides are conventionally classified into two groups, called Dion–Jacobson phases and Ruddlesden–Popper phases, and follow general formulae $A'[A_{n-1}B_nO_{3n+1}]$ and $A'_2[A_{n-1}B_nO_{3n+1}]$, respectively (A' = interlayer alkali metal, A = rare earth or transition metal, B = Ti, Zr, Nb, Ta, etc.) [41–43]. Valuable photocatalytic properties of these materials originate from the unique structure of the perovskite slabs and chemically active interlayer spaces, participating in ion exchange and intercalation reactions [44–48]. Photocatalytic performance of layered perovskite-like oxides is usually improved via cationic and anionic substitution [49–53], the creation of heterojunctions with other inorganic particles [54–63], sensitization with dyes [64], interlayer organic modification [65–73] and exfoliation into nanosheets [74–76]. The latter approach is of special interest since it allows for producing 2D photocatalytic nanomaterials that, on the one hand, retain the perovskite structure and corresponding valuable physical–chemical properties, and on the other hand, have a number of advantages over bulk precursors. First of all, perovskite nanosheets are characterized by small size and a high specific surface area, which reduces the volume recombination of photogenerated charge carriers, magnifies the amount of active sites, provides efficient adsorption of the reactants and increases the sedimentation stability of the reaction suspension in general [74]. As a consequence, nanosheet-based photocatalysts, as a rule, significantly outperform bulk counterparts in the exhibited activity. In addition, perovskite nanosheets may serve as building blocks for designing new nanostructured photocatalysts via controllable self-assembly [77].

The most common method for producing perovskite nanosheets is the liquid-phase exfoliation of layered precursors in the solutions of bulky organic bases (usually tetrabutylammonium hydroxide, TBAOH) [78]. Prior to the exfoliation, the alkaline forms of the oxides are transformed into the protonated ones ($A' = H$) via acid treatment that, in turn, are dispersed in aqueous TBAOH. Tetrabutylammonium cations TBA^+ penetrate into the oxide interlayer space, leading to its pronounced expansion, which facilitates further incorporation of water molecules from the solution and, as a consequence, swelling of the layered precursor. Then, the suspension is usually exposed to ultrasonic treatment resulting in the delamination of the swollen sample into separate nanosheets [75]. Since the Dion–Jacobson phases demonstrate relatively high reactivity of the interlayer space and are amenable to direct incorporation of relatively large organic structures, their liquid-phase exfoliation has been studied quite well [79–87] and there exist an imposing number of articles on photocatalytic properties of their nanosheets [88–97]. At the same time, the available literature hardly covers the photocatalytic performance of the exfoliated Ruddlesden–Popper phases $HLnTiO_4$ and $H_2Ln_2Ti_3O_{10}$ [98–100], possessing a perovskite slab thickness of $n = 1$ and $n = 3$ titanium-oxygen octahedra, respectively, although bulk forms of these titanates were used to yield efficient hydrogen evolution photocatalysts [67–71]. Apparently, the main difficulty consists in low exfoliation efficiency of the protonated titanates using the conventional TBAOH-assisted approach because of their inability to accommodate directly bulky TBA^+ cations. However, as shown in our previous publications, this obstacle can be overcome by using amine-intercalated forms instead of protonated ones as precursors for exfoliation [101,102], which opens the way to the creation of photocatalysts based on $HLnTiO_4$ and $H_2Ln_2Ti_3O_{10}$ nanosheets.

Another important issue that remained practically unaddressed in the literature until recently [103] is related to the form in which nanosheets should be used as hydrogen evolution photocatalysts. Over the years, the most common approach included flocculation of the nanosheets after liquid-phase exfoliation by strong electrolytes (acids [52,58,88,91,95–97,104,105], alkalis [76] or salts [92–94,106–108]) to obtain standard powder photocatalysts for subsequent redispersing in a desired reaction medium. Meanwhile, our recent study on photocatalytic activity of exfoliated Dion–Jacobson niobates $HA_2Nb_3O_{10}$ (A = Ca, Sr) [103] has revealed a strong influence of the nanosheet form (pristine, reassembled by filtering, reassembled by an acid) on hydrogen production efficiency. Particularly, in most cases the pristine nanosheets without reassembly demonstrated the best performance due to their high active surface area. At the same time, among the reassembled samples, simply filtered nanosheets exhibited a much higher activity than their counterparts precipitated by hydrochloric acid, which, apparently, was associated with greater redispersibility of the former in aqueous media.

The present paper, being a logical continuation of our aforementioned reports [102,103], is a first systematic study on photocatalytic activity of exfoliated Ruddlesden–Popper titanates $HLnTiO_4$ and $H_2Ln_2Ti_3O_{10}$ in the reactions of hydrogen generation from aqueous methanol and pure water. The nanosheets are tested both in as-prepared form after liquid-phase exfoliation and after reassembly by two methods with subsequent redispersing in the reaction solution. The photocatalytic performance of the nanosheets is improved via their surface decoration with nanoparticles of a Pt cocatalyst. Besides this, special attention is paid to consideration of the relationship between the features of the nanosheet-based photocatalysts and their hydrogen evolution activity.

2. Materials and Methods

Here and below, the following abbreviations are used: HLT and HNT for $n = 1$ titanates $HLaTiO_4$ and $HNdTiO_4$; HLT_3 and HNT_3 for $n = 3$ titanates $H_2La_2Ti_3O_{10}$ and $H_2Nd_2Ti_3O_{10}$; $HLT \times EtNH_2$, $HNT \times EtNH_2$, $HLT_3 \times EtNH_2$ and $HNT_3 \times EtNH_2$ for their ethylamine-intercalated derivatives. The three forms of the nanosheets are designated as follows: NSs for pristine (as-prepared) nanosheets without reassembly; filtered NSs for those isolated via simple filtering; HCl-restacked NSs for those isolated via flocculation by hydrochloric acid. The abbreviations for platinized photocatalysts are appended with a /Pt sign at the end.

2.1. Synthesis of Precursors for Exfoliation

Taking into account the data from our recent article [102], ethylamine-intercalated forms of the titanates $HLT \times EtNH_2$, $HNT \times EtNH_2$, $HLT_3 \times EtNH_2$ and $HNT_3 \times EtNH_2$ were used as precursors for the liquid-phase exfoliation into nanosheets. The detailed procedure for preparing the initial compounds is presented in Information S1. Briefly, alkaline layered perovskite-like titanates $NaLnTiO_4$ and $K_2Ln_2Ti_3O_{10}$ (Ln = La, Nd) were synthesized via the conventional ceramic technique and then transformed into the corresponding protonated forms HLT (HNT) and HLT_3 (HNT_3) via the acid treatment that, in turn, were treated with aqueous ethylamine to produce the desired amine-intercalated derivatives.

2.2. Exfoliation into Nanosheets and Their Reassembly

To prepare the suspensions of pristine titanate nanosheets (NSs), 63 mg of each ethylamine derivative was placed into a tube with 50 mL of 0.004 M aqueous TBAOH and sonicated by a 200 W Hielscher UP200St homogenizer (Teltow, Germany) at a half power for 5 min. The precursor and TBAOH amounts were chosen in such a way as to provide a 1:1 ratio of TBA^+ cations to interlayer vertices of perovskite octahedra, which was found to be optimal in terms of the exfoliation efficiency [102]. After shaking at room temperature for 7 d, the mixtures were sonicated for 5 min again. Afterwards, bulk non-exfoliated particles were sedimented using a laboratory centrifuge ELMI CM-6MT (Riga, Latvia) at a separation factor F = 1000 for 1 h and the target suspensions of the nanosheets were carefully separated from the precipitates with a pipette. The exfoliation experiments were repeated several times to prepare the required suspension volumes. Concentrations of the nanosheets in the final suspensions were determined spectrophotometrically using calibration plots from our previous report [102].

Filtered NSs were obtained via the vacuum filtration of the aforementioned suspensions on hydrophilic membrane Teflon filters with a pore size of 200 nm at a rate of 50 mL of the suspension per one filter. The samples were rinsed with an excess of hot water, dried in air and removed from the filters with a spatula.

To obtain HCl-restacked NSs, the suspensions of the exfoliated titanates were acidified by a 1 M hydrochloric acid under continuous stirring to cause the formation of a flocculent precipitate (pH < 7), which was then filtered, rinsed and collected as described above. A generalized scheme for obtaining three forms of the titanate nanosheets is shown in Figure 1.

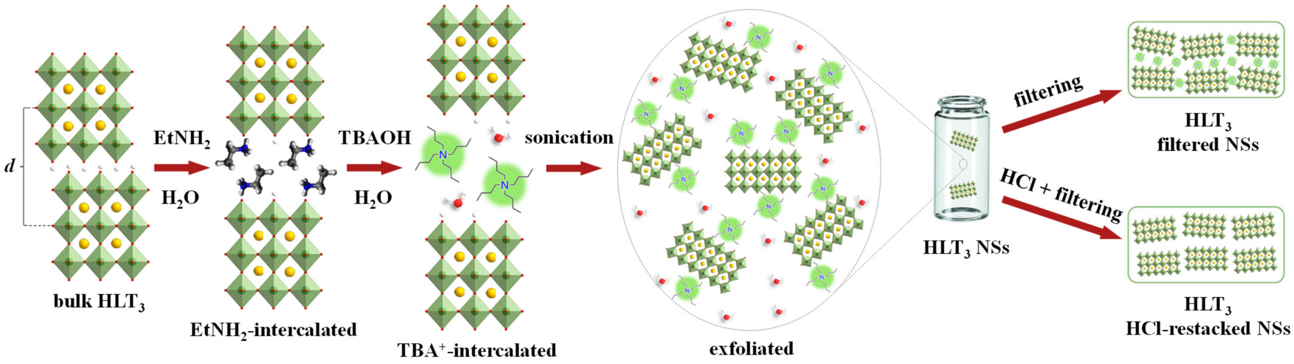

Figure 1. Exfoliation of the titanates into nanosheets and two approaches to their reassembly.

2.3. *Investigation of Photocatalytic Activity and Stability*

Photocatalytic activity was studied in the reactions of light-driven hydrogen production from 1 mol.% aqueous methanol as well as pure water under middle and near ultraviolet irradiation (a 125 W mercury lamp with a light filter transmitting $\lambda > 220$ nm) on the laboratory photocatalytic setting used in our previous reports [65–73]. The main aim was to compare the activity of three forms of exfoliated titanates—pristine, filtered and HCl-restacked nanosheets—with each other and with the protonated precursors. All the samples were tested both in a bare state and after in situ surface modification with a 1% Pt cocatalyst. The default photocatalyst concentration was 500 mg/L with a suspension volume of 50 mL. When investigating the activity of pristine NSs in the presence of TBAOH, the suspensions were preliminarily acidified to achieve pH $\approx$ 6. The default measurement duration was 2 h, after which the lamp was turned off to organize a dark stage and make sure that the photocatalytic reaction stops. The measurements included determination of the hydrogen generation rate ω, apparent quantum efficiency φ and the factor of increase in the reaction rate after platinization k_{Pt} as quantitative indicators of the photocatalytic performance. Actual volume photocatalyst concentrations and pH values were controlled at the beginning (c_1, pH_1) and at the ending (c_2, pH_2) of each experiment. Stability of the suspensions in the course of photocatalytic experiments was evaluated spectrophotometrically by the c_2/c_1 ratio. Long-term stability of the most active photocatalysts was studied in the reaction of hydrogen production from aqueous methanol via performing several running cycles with total duration of 12 h. The activity of the samples obtained was compared with that of the commercial photocatalyst TiO_2 P25 Degussa measured under the same conditions. Composition of some final photocatalytic solutions was additionally analyzed by means of Raman spectroscopy after filtering the dispersed photocatalysts.

The detailed procedure for the photocatalytic measurements, processing experimental results, description of the experimental setting and method for calculation of the lamp photon flux are presented in Information S2–S4. The emission spectrum of the lamp is shown in Figure S1.

2.4. Instrumentation and Data Processing

2.4.1. XRD

Powder X-ray diffraction (XRD) patterns of the samples were obtained on a Rigaku Miniflex II benchtop Röntgen diffractometer (Tokyo, Japan) using Cu K_α radiation, an angle range 2θ = 3–60° and a scanning rate of 10°/min. Indexing of the diffraction patterns and calculation of the lattice parameters were performed on the basis of all the reflections observed using DiffracPlus Topas 4.2 software (Bruker, Karlsruhe, Germany).

2.4.2. Raman Spectroscopy

Raman spectra of the solid samples were recorded on a Bruker Senterra spectrometer (Billerica, MA, USA) in the spectral range of 50–4000 cm^{-1} using a 532 nm solid-state laser (power 2 mW, single accumulation time 60 s, 4 repetitions). Raman spectra of the solutions were collected in the range of 80–3700 cm^{-1} with a 785 nm laser (power 100 mW, single accumulation time 60 s, 8 repetitions).

2.4.3. TG

Thermogravimetric (TG) analysis was performed on a Netzsch TG 209 F1 Libra thermobalance (Selb, Germany) in a synthetic air atmosphere. The temperature program included heating from room temperature to 950 °C at a rate of 10 °C/min followed by a 20 min isotherm at 950 °C to achieve establishing the constant mass.

2.4.4. CHN-Analysis

The carbon, hydrogen and nitrogen content in the reassembled nanosheets was determined via the elemental CHN-analysis on a Euro EA3028-HT analyzer (EuroVector, Pavia, Italy).

2.4.5. DRS

Diffuse reflectance spectra (DRS) were recorded on a Shimadzu UV-2550 spectrophotometer (Kyoto, Japan) with an ISR-2200 integrating sphere in the range of 220–800 nm after sample deposition on a barium sulfate substrate. The reflectance spectra were transformed into coordinates $(F \cdot h\nu)^{1/2} = f(h\nu)$, where $F = (1 - R)^2/(2R)$ is the Kubelka–Munk function of a reflection coefficient R. Linear sections of low-energy regions of the Kubelka–Munk graphs were extrapolated to the intersection point whose abscissa was considered the optical bandgap energy E_g.

2.4.6. TR-PLS

Time-resolved photoluminescence spectroscopy (TR-PLS) was performed on a Horiba Jobin Yvon Fluorolog-3 spectrofluorometer (Kyoto, Japan). The samples were excited by a 265 nm pulse light-emitting diode and the photoluminescence decays were measured at the photoemission maxima. The reassembled titanates were investigated using the signal deconvolution. The decay graphs $I = I(t)$ were fitted by the function $I = A_1 \cdot \exp(-t/t_1) + A_2 \cdot \exp(-t/t_2) + I_0$ and average photoluminescence lifetimes τ were found via the formula $\tau = (A_1 \cdot t_1{}^2 + A_2 \cdot t_2{}^2)/(A_1 \cdot t_1 + A_2 \cdot t_2)$.

2.4.7. SEM

Morphology of the bulk protonated titanates and reassembled nanosheets was investigated on a Zeiss Merlin scanning electron microscope (SEM) (Oberkochen, Germany) equipped with a field emission cathode, electron optics column Gemini II and oil-free vacuum system.

2.4.8. BET

Specific surface areas S were measured on a Quadrasorb SI adsorption analyzer (Boynton Beach, FL, USA). Prior to the analysis, 100–150 mg of each sample was degassed at 25 °C for 12 h. Adsorption isotherms were measured at a liquid nitrogen temperature (−196 °C) with nitrogen as an adsorbate. The values of specific surface area were calculated via the conventional multipoint Brunauer–Emmett–Teller method (BET).

2.4.9. Laser Granulometry

Particle size distributions for the reassembled nanosheets were roughly estimated on a laser diffraction particle size analyzer Mastersizer 3000 (Malvern Panalytical, Malvern, UK) after their dispersing in water with a Hydro MW sonication unit, using the Mie scattering model and a particle refractive index of 2.51.

2.4.10. UV-Vis Spectrophotometry

Nanosheet concentrations after liquid-phase exfoliation and stability of the reaction suspensions during photocatalytic experiments were controlled via the spectrophotometric analysis carried out on a Thermo Scientific Genesys 10S UV-Vis spectrophotometer (Waltham, MA, USA). The spectra were recorded in the range of 190–1100 nm at optical density $A < 2$. The 1 mol.% aqueous methanol or pure distilled water were used for dilution and baseline subtraction. The concentrations were calculated using spectrophotometric calibration plots from our previous report [102].

2.4.11. pH-Metry

The pH values of the reaction suspensions were controlled using a laboratory pH-meter Mettler Toledo SevenCompact S220 (Greifensee, Switzerland) equipped with an InLab Expert Pro-ISM electrode.

3. Results and Discussion

3.1. Characterization of the Initial Titanates, Their Pristine and Reassembled Nanosheets

Successful preparation of the initial protonated titanates and their ethylamine-intercalated derivatives was confirmed by means of powder XRD analysis, similar to our previous reports [69,109]. All the diffraction peaks were indexed and the calculated tetragonal lattice parameters were found to be in good agreement with the values reported earlier (PDF cards 01-075-2761, 01-076-3080, 00-048-0983 and 01-087-0479). The insertion of ethylamine provided significant expansion of the titanates' interlayer space and corresponding increase in the interlayer distance d (defined in Figure 1). As established in our previous publication [102], the ethylamine pre-intercalation is a vital step to achieve acceptable nanosheet yields during the subsequent liquid-phase exfoliation of the titanates under study in view of their inability to accommodate bulky TBA^+ cations directly.

The use of the ethylamine precursors allowed obtaining suspensions of titanate nanosheets (NSs) with the solid phase concentrations (yields) of 250 mg/L (25%), 930 mg/L (93%), 740 mg/L (74%) and 890 mg/L (89%) for HLT, HNT, HLT_3 and HNT_3, respectively. Comprehensive characterization of the pristine titanate NSs before reassembly by means of UV-vis spectrophotometry, dynamic light scattering, electron and atomic force microscopy is presented in our previous paper [102]. Briefly, the samples preserve the original structure of perovskite slabs upon the exfoliation and resulting NSs represent mainly rectangular particles with lateral dimensions of 30–250 nm. Their predominant thickness is 2.0–2.5 nm, which corresponds to the titanate monolayer (one perovskite slab). Along with monolayers, the suspensions also contain bilayer particles with the thickness of 4.0–4.5 nm, but in significantly smaller quantities. Initial pH of the nanosheet-containing suspensions is ≈11.7, which may be too high for their catalytic and photocatalytic applications and may require additional acidification. Meanwhile, aggregative and sedimentation stability of these suspensions was shown to be strongly pH-dependent. In particular, the first visible signs of the nanosheet agglomeration appear at pH $\leq$ 9.5 and, when pH is below 8.0 (for HLT and HNT NSs) or 7.5 (for HLT_3 and HNT_3 NSs), the particles experience flocculation and gradual sedimentation unless the stirring is switched on. In general, the suspensions of the titanate show lower stability with respect to acidification than those of the exfoliated niobates $HA_2Nb_3O_{10}$ (A = Ca, Sr) investigated earlier [103], which are stable as long as the pH is greater than 4–5.

Using the suspensions of pristine NSs, two forms of the reassembled titanates (filtered NSs and HCl-restacked NSs) were also successfully collected. As in the case of the niobates $HA_2Nb_3O_{10}$ (A = Ca, Sr) [103], the direct filtration has proven to be a much less convenient approach to the nanosheet isolation from a practical point of view than the reassembly by hydrochloric acid. Particularly, the filtered NSs quickly clog the membrane filter pores and the filtration process takes a very long time. The suspension acidification, on the contrary, gives a flocculent precipitate of HCl-restacked NSs that practically does not clog the filter, allowing for a much higher filtration rate. Apparently, this is why the sedimentation by strong electrolytes remains the most common approach to the isolation of layered oxide nanosheets in the available literature. However, as will be shown below, the isolation approach used significantly influences the properties of the reassembled samples.

Primary characterization of the reassembled titanates was performed using powder XRD analysis (Figure 2, Table 1). As one can see from the patterns obtained, both forms of the reassembled nanosheets exhibit evident reflections (00x), corresponding to large interplanar distances between the stacked layers. Moreover, the samples preserve practically the same positions of (110) and (020) reflections as well as values of the *a* lattice parameter as their bulk precursors. At the same time, XRD patterns of the reassembled samples differ noticeably from those of the precursors in strong broadening of the diffraction maxima, which points to the expressed nanosheet stacking disorder. Thus, both simple filtration and restacking of the nanosheets by hydrochloric acid result in the assembly of the layered perovskite-like structure with lower orderliness than in the case of the initial protonated titanates. Meanwhile, all the reassembled samples show a pronounced low-angle shift in the (00x) reflections and, accordingly, possess greater interlayer distances *d* in comparison with those of the protonated precursors (Figure 2, Table 1). This observation points to the existence of some factors preventing the interlayer space from stronger contraction, such as potential interlayer embedding of TBA^+ cations and water molecules. Moreover, it is important to notice that in the case of HLT_3 and HNT_3 titanates, filtered NSs are characterized by a more expanded interlayer space than their HCl-restacked counterparts.

Raman spectra of the reassembled nanosheets (Figure 3) demonstrate immutability of most vibrational modes located in the titanium–oxygen octahedra (400–750 cm^{-1}) and in the $(LnO)_2$ layer (270–320 cm^{-1}, for HLT and HNT only) once again indicating preservation of the perovskite structure upon exfoliation and reassembly. The main exception is the symmetric stretching mode of axial Ti–O bonds directed towards the ion-exchangeable interlayer space (≈835 cm^{-1} for HLT, HNT and ≈820 cm^{-1} for HLT_3, HNT_3) whose frequency is known to be sensitive to the interlayer composition. When going from the protonated titanates to their reassembled forms, the aforementioned band evidently splits into two new intense ones: ≈775 and ≈890 cm^{-1} for HLT (HNT) filtered NSs, ≈780 and ≈905 cm^{-1} for HLT (HNT) HCl-restacked NSs, ≈760 and ≈900 cm^{-1} for HLT_3 (HNT_3) filtered NSs and ≈765 and ≈910 cm^{-1} for HLT_3 (HNT_3) HCl-restacked NSs. Such splitting, apparently, should originate from some changes in the surrounding of the interlayer oxygen vertices of the terminal perovskite octahedra. Moreover, the foregoing split bands in the filtered NSs exhibit 5–15 cm^{-1} lower frequencies than in the HCl-restacked ones, which may point to stronger association of the oxygen vertices with the interlayer components. A similar splitting caused by the partial dissociation of interlayer hydroxyl groups of the oxide and subsequent protonation of amine molecules in the interlayer space was observed earlier for the amine-intercalated titanates [69,109]. Furthermore, Raman spectra of the filtered NSs clearly show the presence of TBA^+ cations in these samples: one can see the bands of C–N (≈1040 cm^{-1}), C–C (≈1060 cm^{-1}) and C–H (2820–3050 cm^{-1}) stretching, C–C–H (≈1130 cm^{-1}) and C–N–C (≈1450 cm^{-1}) bending as well as H–C–H wagging (≈1310 and ≈1450 cm^{-1}). Thus, the TBA^+ cations appear to be relatively strongly associated with the nanosheets, which prevents their complete washout when rinsing with an excess of hot water. Additionally, the vibrational bands of TBA^+ are seen to be more intense in the spectra of HLT_3 and HNT_3 filtered NSs, which could indicate greater content of the organics in these samples. The HCl-restacked NSs, on the contrary, give barely noticeable TBA^+ signals, comparable in intensity with those of water being a weak Raman scatterer. This suggests that an amount of the residual organics in the HCl-restacked NSs should be significantly lower.

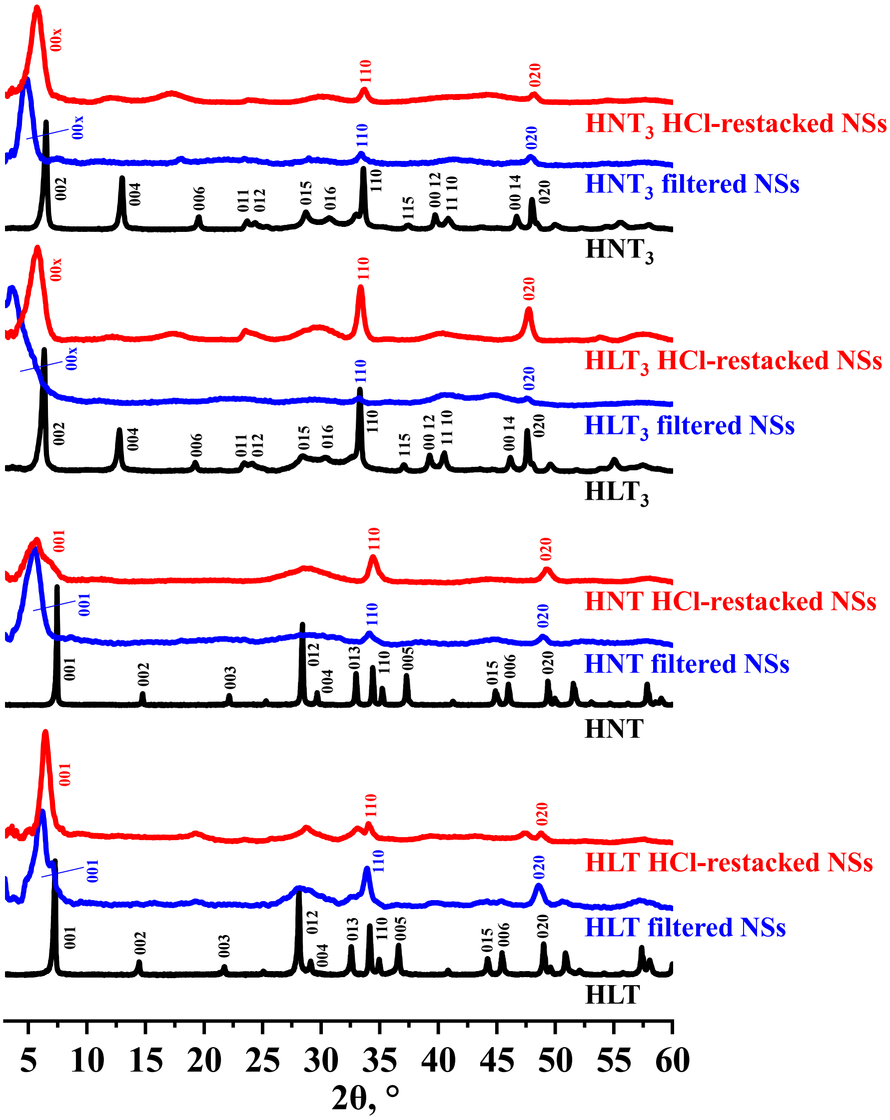

Figure 2. XRD patterns of the protonated titanates and their reassembled nanosheets.

Table 1. Characterization of the protonated titanates and their reassembled nanosheets: tetragonal lattice parameters (*a*, *c*), interlayer distances (*d*), quantitative compositions (x, y for $H_{1-x}LnTiO_4 \cdot xTBA \cdot yH_2O$ and $H_{2-x}Ln_2Ti_3O_{10} \cdot xTBA \cdot yH_2O$), light absorption regions (optical bandgap energies E_g, absorption edges λ_{abs}), average photoluminescence lifetimes (τ) measured with 265 nm excitation at emission maxima (λ_{em}), specific surface areas (S).

Sample	*a*, Å	*c*, Å	*d*, Å	x	y	E_g, eV	λ_{abs}, nm	τ, µs (λ_{em}, nm)	S, m^2/g
HLT	3.7	12.2	12.2	–	0.05	3.45	359	4.70 (360)	9.7
HLT filtered NSs	≈3.7	≈14.0	≈14.0	0.05	0.40	3.40	365	0.0071 (420)	54
HLT HCl-restacked NSs	≈3.7	≈14.0	≈14.0	0.02	0.40	3.25	382	–	73
HNT	3.7	12.1	12.1	–	0.10	3.48	356	4.77 (360)	8.6
HNT filtered NSs	≈3.7	≈16.0	≈16.0	0.05	0.45	3.22	385	0.0042 (420)	64
HNT HCl-restacked NSs	≈3.7	≈16.0	≈16.0	0.01	0.75	3.29	377	–	85
HLT$_3$	3.8	27.2	13.6	–	0.15	3.45	359	4.73 (370)	3.2
HLT$_3$ filtered NSs	≈3.8	≈24.0	≈24.0	0.20	0.60	3.26	380	0.0081 (430)	21
HLT$_3$ HCl-restacked NSs	≈3.8	≈15.5	≈15.5	0.02	1.10	3.34	371	0.0063 (430)	60
HNT$_3$	3.8	27.2	13.6	–	0.15	3.47	357	5.42 (370)	3.1
HNT$_3$ filtered NSs	≈3.8	≈19.5	≈19.5	0.20	1.20	3.26	380	0.0075 (430)	15
HNT$_3$ HCl-restacked NSs	≈3.8	≈15.5	≈15.5	0.02	1.20	3.22	385	0.0058 (430)	47

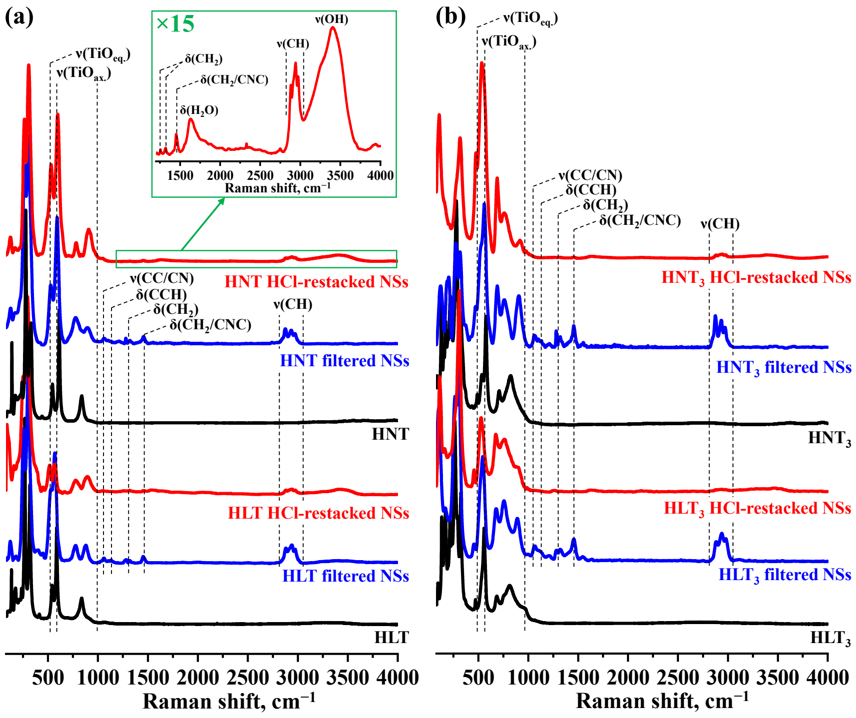

Figure 3. Raman spectra of the *n* = 1 (**a**) and *n* = 3 (**b**) protonated titanates and their reassembled nanosheets.

To confirm the assumption about the residual TBA^+ content, the quantitative compositions of the reassembled samples were investigated by means of TG (Figure S2) and elemental CHN-analysis. TG curves of the initial protonated titanates demonstrate two clearly distinguishable mass loss stages corresponding to the liberation of intercalated water molecules (below 250–300 °C) and subsequent decomposition of the anhydrous protonated compound (above 275–300 °C). The curves of the reassembled nanosheets, on the contrary, exhibit a more gradual mass decrease consisting of several overlapping stages that are difficult to delimitate. Total mass losses for all the reassembled samples are several times greater than those for the protonated titanates. Approximately a half of each mass loss takes place at relatively low temperatures (below 150–200 °C), which allows it to attribute predominantly to the liberation of water located between the stacked nanosheets. Additionally, the filtered NSs give greater total mass losses than their HCl-restacked counterparts indicating a higher content of TBA^+ cations and/or water molecules. Indeed, combined TG and CHN-analysis data allow for finding the organic content of 0.05 and 0.20 TBA^+ cations per the titanate formula unit for HLT (HNT) and HLT_3 (HNT_3) filtered NSs, respectively, as well as a perceptible amount of embedded water (0.40–1.20 molecules) (Table 1). At the same time, the HCl-restacked NSs contain only 0.01–0.02 TBA^+ cations per the formula unit, which is in good agreement with relatively low intensity of the corresponding bands in their Raman spectra (Figure 3). With that said, the filtered NSs can in some sense be considered hybrid inorganic–organic compounds with TBA^+ cations strongly embedded between the stacked nanosheets. Unlike them, the HCl-restacked NSs are practically devoid of the residual organics that, apparently, are washed out in the form of tetrabutylammonium chloride during the suspension acidification and further sample rinsing.

The light absorption range of the samples was studied using DRS with the Kubelka–Munk transformation (Figure 4). It is easy to see that both protonated titanates and their reassembled nanosheets have the long-wave edge of intrinsic absorption lying in the near-ultraviolet spectrum area. Nd-containing samples additionally demonstrate several absorption peaks in the visible region that are not due to the interband transition but due to Nd^{3+} own energy levels. It is these absorption peaks that explain the lilac color of Nd-containing titanates while their La-containing counterparts are white (colorless). However, the most important fact established by DRS is the bandgap narrowing observed when going from the initial protonated samples to their reassembled nanosheets (Table 1), which allows corresponding photocatalysts to absorb more light for promoting target reactions. For instance, the optical bandgap energy E_g of HNT and HNT_3 is reduced from 3.47–3.48 to 3.22 eV upon exfoliation and reassembly, so the final samples are formally able to utilize irradiation with wavelengths up to 385 nm while the initial compounds are limited by the values of 356–357 nm.

The intensity of radiative electron–hole recombination in the samples was studied using the TR-PLS method (Figures 5 and S3). The photoluminescence spectra measured with a 265 nm excitation evidenced a pronounced bathochromic shift in the reassembled nanosheets' emission maxima (by ≈60 nm) in comparison with those of the initial protonated titanates. Next, the samples were excited by a 265 nm pulse light-emitting diode and the photoluminescence decays were detected at the emission maxima. When the chosen excitation wavelength falls in the area of intrinsic photocatalyst absorption and the recombination is assumed to be predominantly radiative, the average lifetime of photoluminescence τ should correlate with that of the photogenerated charge carriers. In our case, τ values for the initial protonated titanates turned out to be in the range of 4.7–5.4 μs (Table 1). At the same time, their reassembled forms exhibited noticeably poorer photoluminescence lifetimes of 0.0042–0.0081 μs, which may be due, among other things, to the relatively disordered nature of these samples facilitating the luminescence quenching. Nevertheless, a strict comparison of the reassembled titanates with the precursors is hardly acceptable here since their luminescence spectra are strongly shifted relative to each other and the lifetimes correspond to different emission wavelengths. Meanwhile, the emission maxima of all the reassembled samples are almost the same, which allows one to make some comparisons. As one can see from Table 1, the HLT filtered NSs show a ≈1.7 times greater τ value than HNT filtered ones. In the case of HLT_3 and HNT_3 filtered NSs, this difference is less expressed and does not exceed ≈1.1 times. In addition, the reassembly approach also affects the photoluminescence lifetime: the filtered HLT_3 (HNT_3) NSs provide ≈1.3 times higher τ values in comparison with their HCl-restacked counterparts. Thus, the lowest rate of radiative electron–hole recombination among the reassembled titanates (and ceteris paribus, highest photocatalytic performance) is expected in the case of La-containing nanosheets isolated via direct filtration.

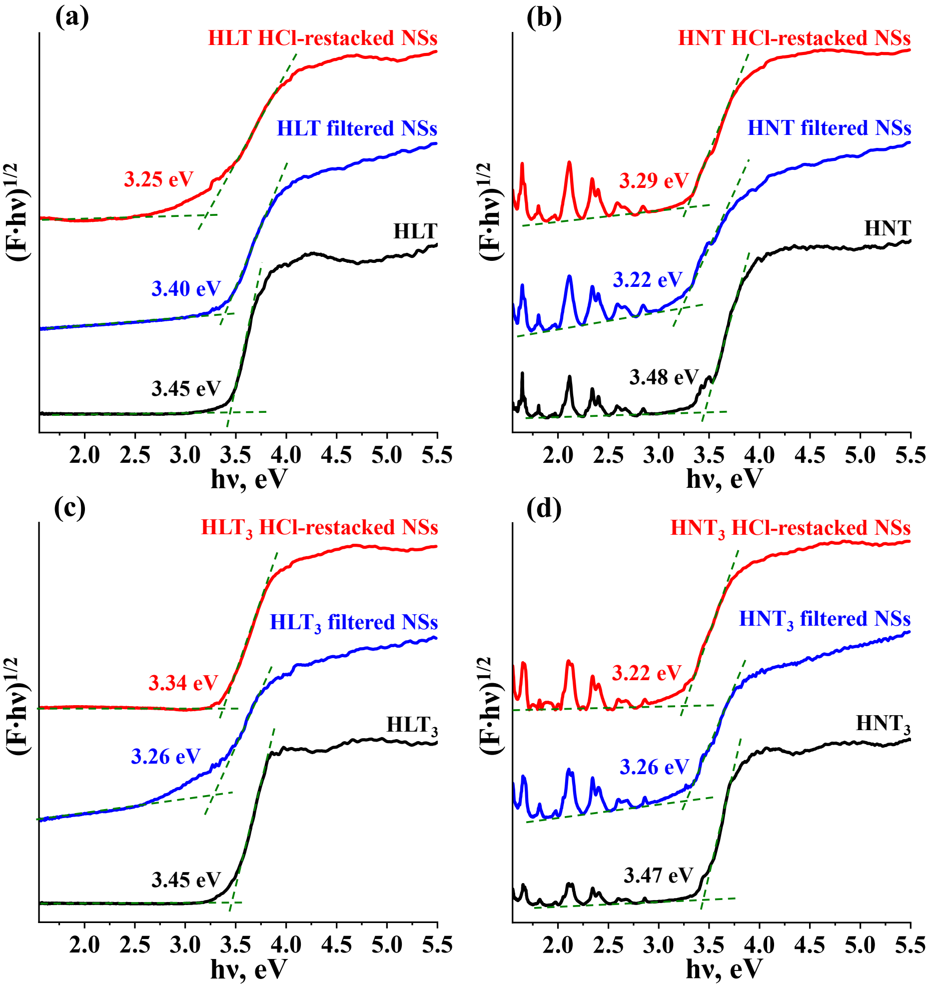

Figure 4. Kubelka–Munk plots for protonated forms and reassembled nanosheets of the titanates HLT (**a**), HNT (**b**), HLT_3 (**c**) and HNT_3 (**d**).

Morphology and the specific surface area of the samples were investigated using SEM and BET methods (Figure 6, Table 1). The initial protonated titanates are seen to represent agglomerates of monolithic lamellar particles with lateral dimensions of 0.5–4 µm and a thickness of 200–600 nm. Their reassembled forms, on the contrary, consist of distorted perovskite layers with irregularly shaped edges, stacked in a relatively large aggregates of micrometer sizes. The reassembled nanosheets of HLT_3 and HNT_3 demonstrate an evidently greater stacking order than those of HLT and HNT and one can clearly observe individual layers of a nanoscale thickness. The specific surface area of the exfoliated and reassembled titanates reaches 85 m^2/g and exceeds that of the precursors (3–10 m^2/g) by up to 19 times, which is of high importance for catalytic applications. Moreover, HLT and HNT samples outperform their HLT_3 and HNT_3 counterparts in the specific surface and the reassembly approach chosen noticeably influences its value: the surface area of HCl-restacked NSs exceeds that of the filtered NSs by ≈1.3 times for HLT (HNT) and ≈3 times for HLT_3 (HNT_3).

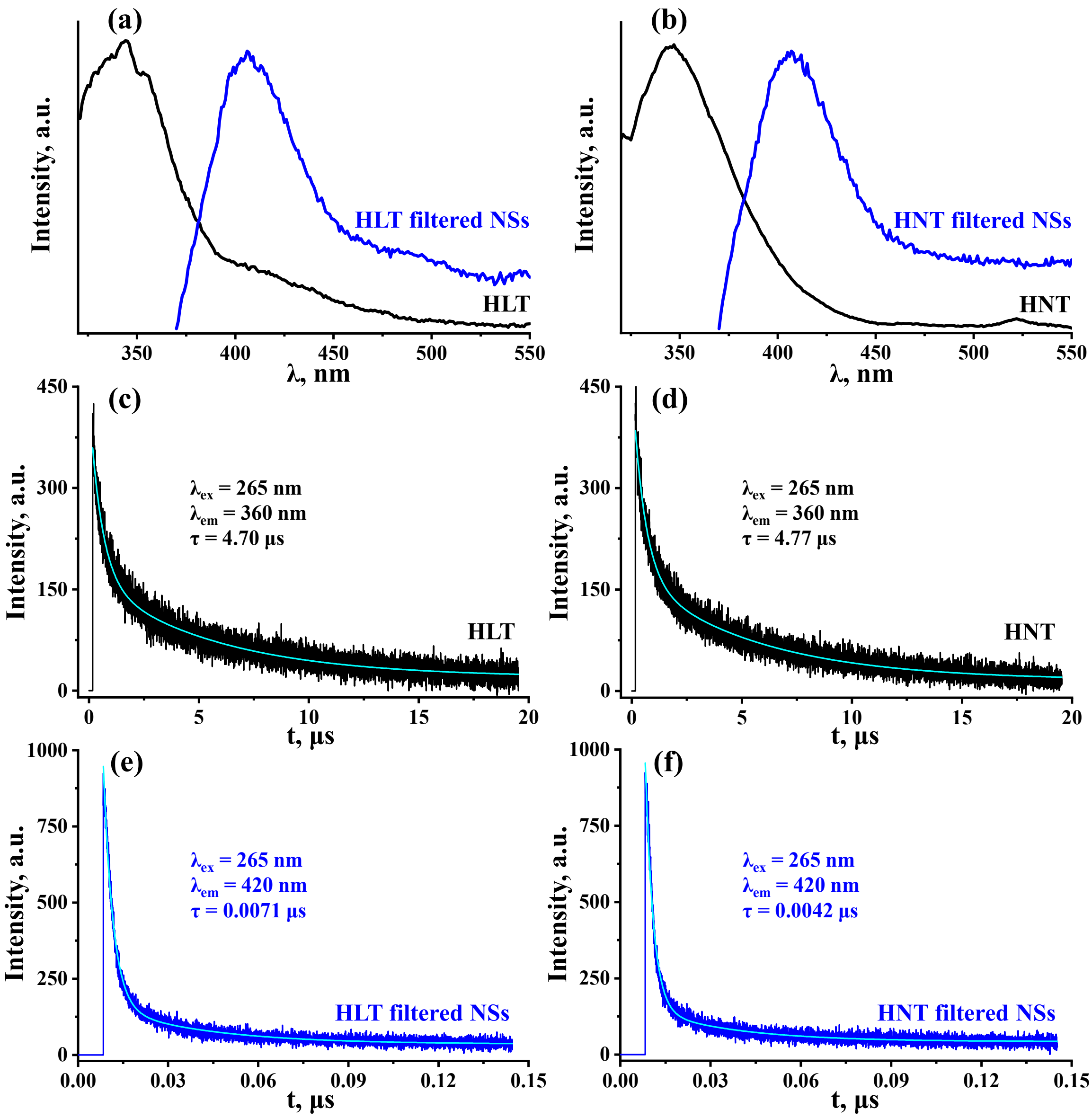

Figure 5. Photoluminescence spectra (**a**,**b**) and decay graphs (**c**–**f**) for the protonated titanates HLT, HNT and their reassembled nanosheets.

Particle sizes of two forms of the reassembled titanates were additionally compared using laser granulometry after their dispersing in water (Figure 7a,b). It should be said right away that this method gives only a rough comparison of the prevailing particle sizes in the samples with each other, but does not allow for strictly judging their absolute values since the calculation theory used is not adapted for lamellar solids. As can be seen from Figure 7a,b, particle size distributions for the HCl-restacked NSs are shifted to the right relative to those for the filtered NSs. Thus, the latter are expected to possess greater specific surfaces due to smaller average particle dimensions, which is not formally consistent with the BET data (Table 1). The reason for this apparent contradiction is that the specific surface area is measured for dry solid samples while the size distributions are obtained after their ultrasonic dispersing in water. Apparently, the filtered NSs undergo the disaggregation much easier than their HCl-restacked counterparts and, thanks to this, have smaller sizes (greater surface area) in a suspended state.

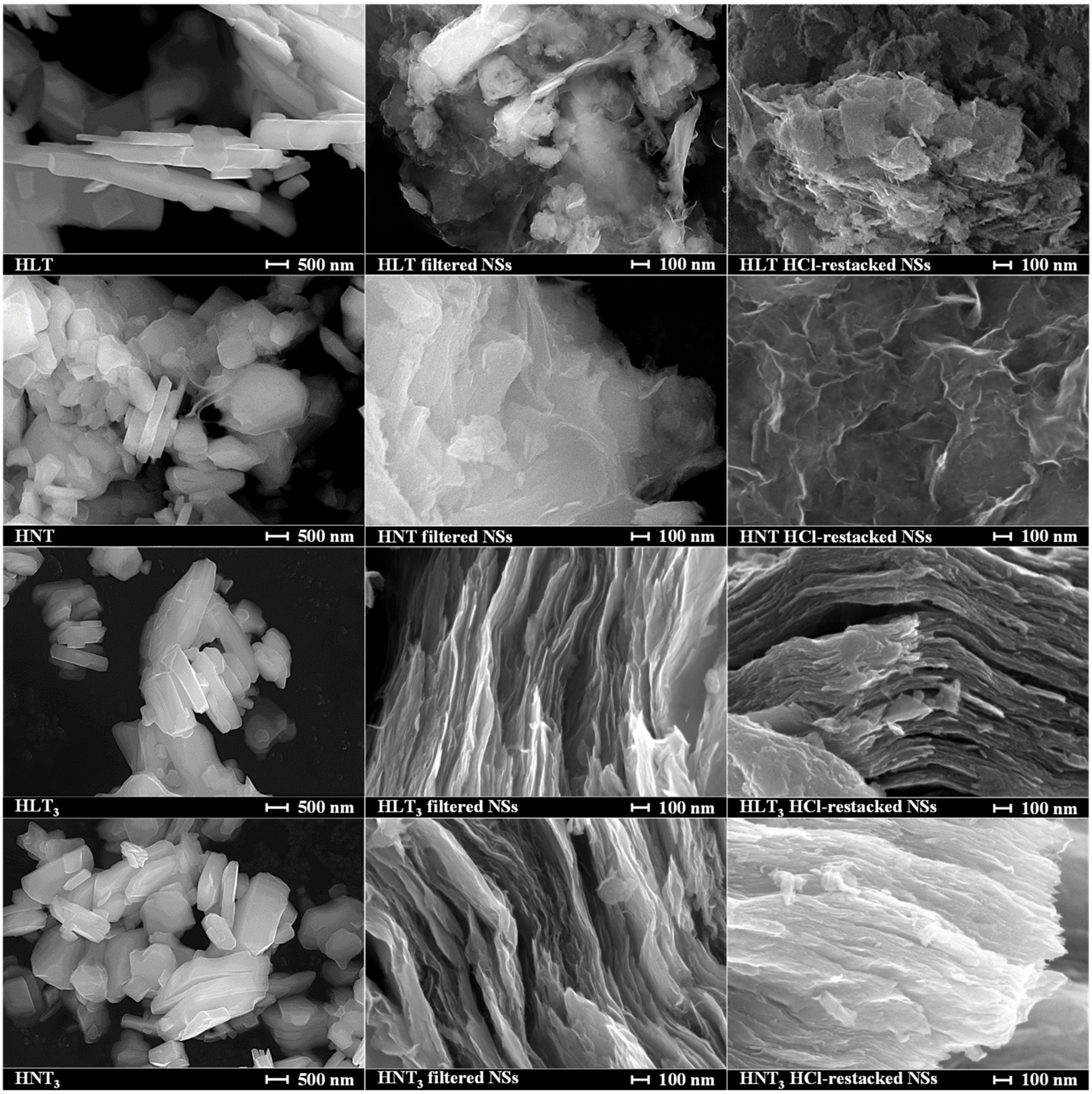

Figure 6. SEM images of the protonated titanates and their reassembled nanosheets.

The relationship between prevailing particle sizes of the initial titanates, their pristine and reassembled nanosheets can also be illustrated by characteristic UV-vis spectra of their aqueous suspensions (Figure 7c,d). The initial protonated samples are seen to give non-zero optical density across the entire spectrum, which is caused by intense Mie scattering on relatively large particles. The suspensions of pristine NSs, on the contrary, show narrow overlapping bands only in the middle-ultraviolet region (200–340 nm), representing a superposition of scattering and absorption by the nanoparticles, while optical density at greater wavelengths tends to zero. The spectra of both forms of the reassembled and redispersed nanosheets represent a cross between those of the bulk precursors and pristine NSs: they show expressed maxima in the ultraviolet range and, at the same time, non-zero optical density in the rest of the spectrum. This allows one to deduce that their average particle sizes occupy an intermediate position between those of the protonated titanates and their pristine NSs. Meanwhile, the spectra of the dispersed filtered NSs differ from those of the HCl-restacked ones by clearer peaks in the ultraviolet area and lower optical density in the visible range. This fact, apparently, points to smaller particle sizes of the filtered NSs and is consistent with the results of laser granulometry (Figure 7a,b).

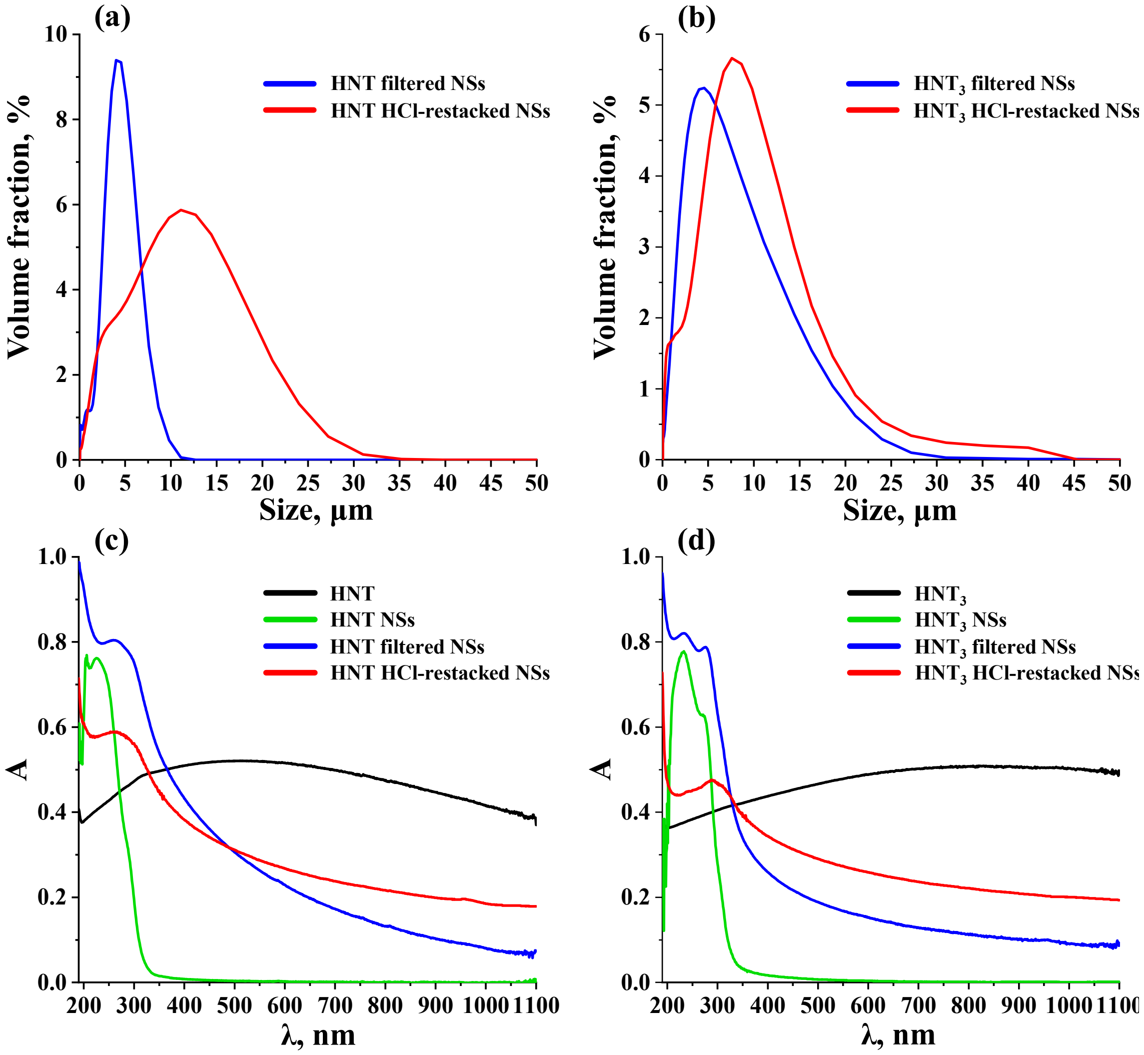

Figure 7. Particle size distributions for the reassembled HLT_3 and HNT_3 nanosheets (**a**,**b**) and typical UV-vis spectra of the suspensions of HLT_3, HNT_3, their pristine as well as reassembled and redispersed nanosheets (**c**,**d**).

Thus, the differences between two forms of reassembled titanate nanosheets—filtered and HCl-restacked ones—are generally the same as described for the analogous forms of the exfoliated niobates $HA_2Nb_3O_{10}$ (A = Ca, Sr) from our previous report [103]. In brief, the filtered NSs, being more time-consuming to obtain, represent in some sense hybrid inorganic–organic materials with TBA^+ cations strongly embedded between the stacked layers. They demonstrate improved charge carrier lifetimes and better dispersibility in aqueous media, which provides smaller sizes of their suspended particles despite a lower specific surface area in a dry state. The HCl-restacked NSs, on the contrary, are more convenient to obtain in large quantities. However, they are practically devoid of the residual organics and show poorer lifetimes of photogenerated electron–hole pairs. Although the HCl-restacked NSs possess higher specific surface areas in a dry form, they are less dispersible in water and give greater particle sizes in the suspensions.

3.2. Photocatalytic Activity in the Reactions of Hydrogen Evolution

The initial protonated titanates and three forms of their nanosheets—pristine, filtered and HCl-restacked—have been comprehensively investigated as heterogeneous photocatalysts of hydrogen production from 1 mol.% aqueous methanol as well as pure distilled water. Each photocatalyst was tested both in a bare state and after in situ surface decoration with 1% Pt nanoparticles. The latter are known to serve as a cocatalyst suppressing the surface charge carrier recombination and creating new active sites of hydrogen formation, which usually leads to noticeably higher photocatalytic activity of the platinized samples [35]. Kinetic curves of hydrogen evolution obtained are shown in Figures 8 and S4–S8, data on the photocatalytic activity are summarized in Table 2 and comparison of the apparent quantum efficiencies φ is visualized as bar graphs in Figure 9. As one can see, practically all the kinetic curves demonstrate linear behavior that confirms a stable hydrogen production rate throughout the whole experiment time. When the light source is switched off, the curves reach a plateau indicating the absence of the activity in a dark mode.

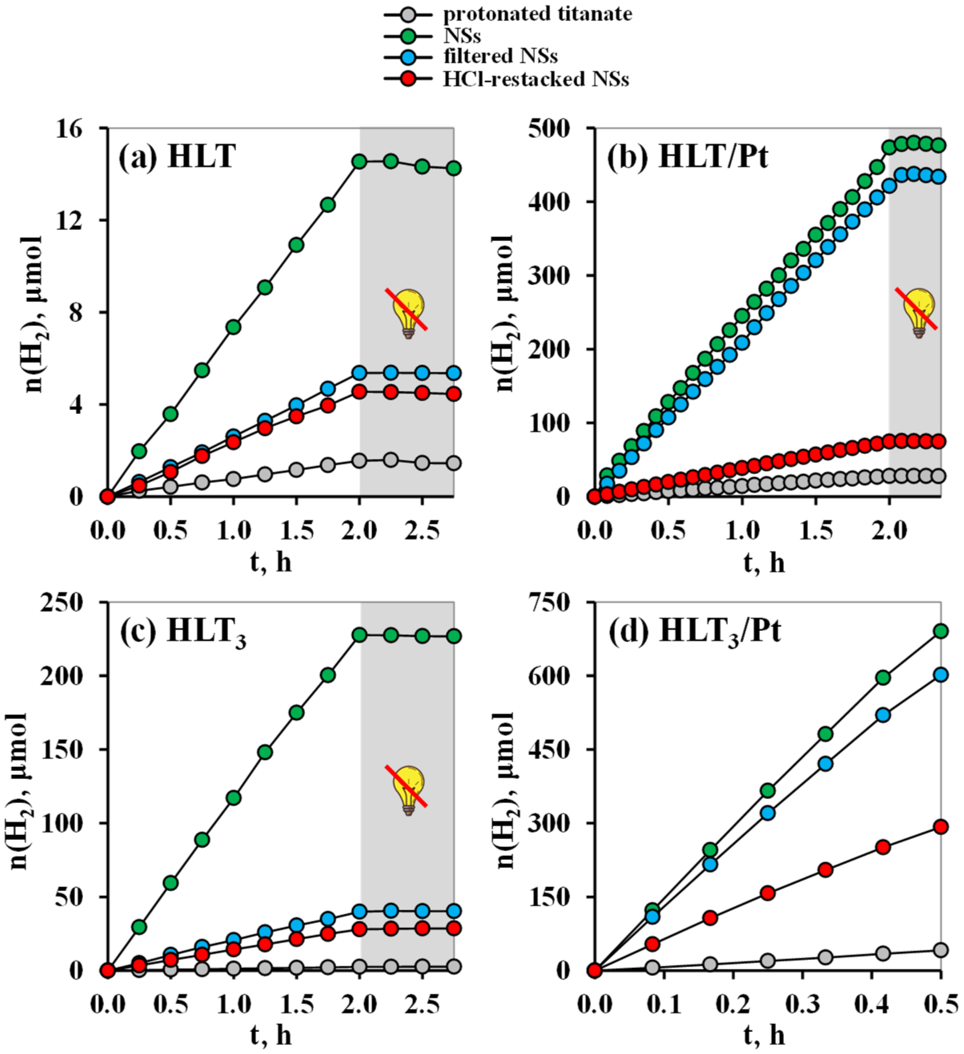

Figure 8. Kinetic curves of photocatalytic hydrogen evolution from 1 mol.% aqueous methanol over the protonated titanates HLT (**a**,**b**), HLT$_3$ (**c**,**d**) and their nanosheet-based photocatalysts.

Table 2. Photocatalytic activity of the protonated titanates and their nanosheets in the reactions of hydrogen evolution: hydrogen production rates (ω), apparent quantum efficiencies (φ), factors of increase in the reaction rate after platinization (k_{Pt}).

Photocatalyst	**1 mol.% CH_3OH**			**H_2O**		
	ω (H_2), μmol/h	**φ, %**	**k_{Pt}**	**ω (H_2), μmol/h**	**φ, %**	**k_{Pt}**
HLT	0.73	0.010	–	0.03	0.0007	–
HLT/Pt	14.2	0.19	19	0.66	0.014	22
HLT NSs	7.21	0.12	–	0.45	0.007	–
HLT NSs/Pt	225	3.72	31	33.2	0.55	74
HLT filtered NSs	2.71	0.045	–	0.34	0.006	–
HLT filtered NSs/Pt	209	3.46	77	15.7	0.26	46
HLT HCl-restacked NSs	2.27	0.023	–	0.24	0.002	–
HLT HCl-restacked NSs/Pt	37.2	0.38	16	8.48	0.087	35
HNT	0.73	0.010	–	0.04	0.0009	–
HNT/Pt	6.23	0.083	8.5	0.11	0.002	2.8
HNT NSs	3.11	0.032	–	0.37	0.004	–
HNT NSs/Pt	11.2	0.12	3.6	0.81	0.008	2.2
HNT filtered NSs	0.94	0.010	–	0.15	0.002	–
HNT filtered NSs/Pt	9.91	0.10	11	0.48	0.005	3.2
HNT HCl-restacked NSs	0.51	0.005	–	0.03	0.0003	–
HNT HCl-restacked NSs/Pt	7.95	0.082	16	0.25	0.003	8.3
HLT_3	1.27	0.017	–	0.08	0.002	–
HLT_3/Pt	85.1	1.14	67	19.7	0.43	246
HLT_3 NSs	112	1.16	–	20.9	0.21	–
HLT_3 NSs/Pt	1370	14.2	12	139	1.42	6.7
HLT_3 filtered NSs	19.6	0.20	–	4.15	0.043	–
HLT_3 filtered NSs/Pt	1190	12.3	61	305	3.15	73
HLT_3 HCl-restacked NSs	14.1	0.14	–	3.01	0.031	–
HLT_3 HCl-restacked NSs/Pt	573	5.91	41	98.6	1.02	33
HNT_3	2.00	0.027	–	0.05	0.001	–
HNT_3/Pt	69.0	0.92	35	15.9	0.35	318
HNT_3 NSs	21.4	0.22	–	2.10	0.022	–
HNT_3 NSs/Pt	1260	13.0	59	70.6	0.73	34
HNT_3 filtered NSs	9.73	0.10	–	1.39	0.014	–
HNT_3 filtered NSs/Pt	523	5.39	54	142	1.46	102
HNT_3 HCl-restacked NSs	8.57	0.088	–	0.58	0.006	–
HNT_3 HCl-restacked NSs/Pt	360	3.70	42	15.0	0.15	26

As follows from Table 2 and has already been shown in previous reports [69,70], the initial protonated titanates exhibit quite modest hydrogen evolution activity from 1 mol.% aqueous methanol. Particularly, bare HLT and HNT samples provide the apparent quantum efficiency of only 0.010%, while HLT_3 and HNT_3 allow achieving 0.017% and 0.027%, respectively. After surface platinization, the hydrogen evolution activity sharply increases reaching the φ values up to 0.19% for HLT/Pt and 1.14% for HLT_3/Pt. These values are noticeably lower than those reported for the niobates $HA_2Nb_3O_{10}$ (A = Ca, Sr) tested under the same conditions (up to 0.48% in a bare form and 7.8% after platinization) [103]. A potential reason for this difference consists in poor hydratability of the protonated titanates (0.05–0.15 water molecules per the formula unit) as compared to that of the niobates (up to 1.5 molecules).

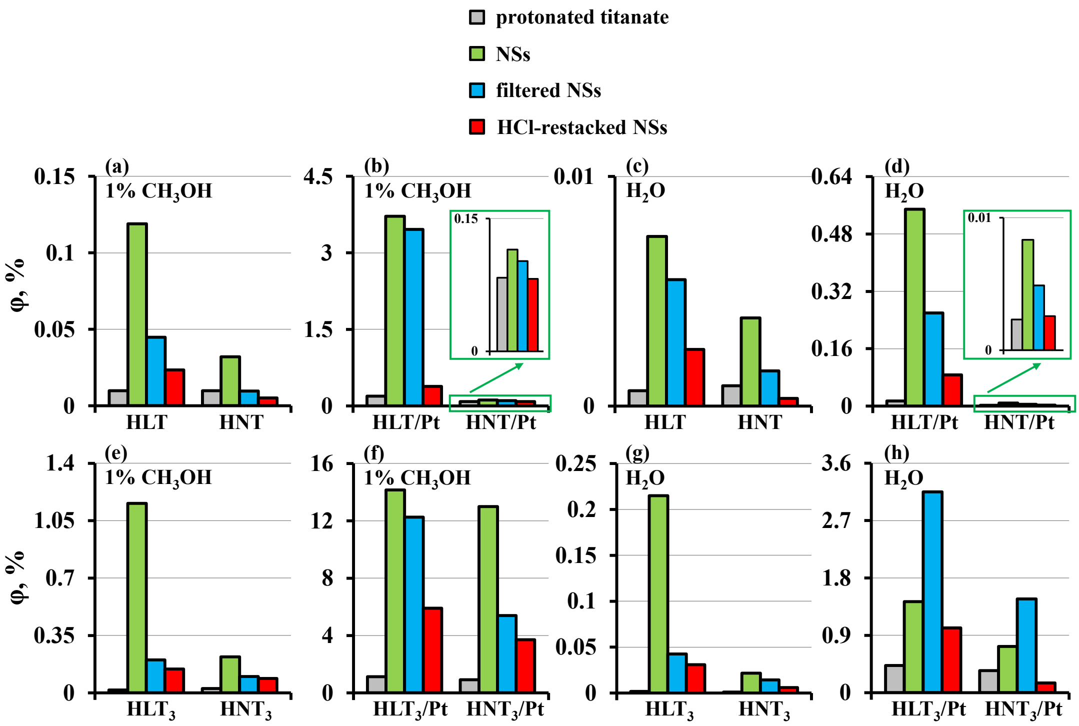

Figure 9. Comparison of apparent quantum efficiency of hydrogen generation from 1 mol.% aqueous methanol and water over n = 1 (**a**–**d**) and n = 3 (**e**–**h**) protonated titanates and their nanosheet-based photocatalysts.

Meanwhile, exfoliation of the titanates into nanosheets leads to great enhancement of the hydrogen production rate from aqueous methanol. Particularly, the pristine NSs outperform the bulk protonated precursors by up to 88 times and, after platinization, demonstrate the quantum efficiency of 3.72% (HLT), 0.12% (HNT), 14.2% (HLT_3) and 13.0% (HNT_3). Furthermore, the activity of HLT NSs/Pt (ω = 225 μmol/h, φ = 3.72%) is the highest hydrogen evolution activity achieved so far over the n = 1 Ruddlesden–Popper titanates $ALnTiO_4$ according to the available literature. The filtered NSs also show acceptable photocatalytic performance being up to 15 times superior to that of the precursors. After their modification with a Pt cocatalyst, the quantum efficiency reaches 3.46% (HLT), 0.10% (HNT), 12.3% (HLT_3) and 5.39% (HNT_3). However, the HCl-restacked NSs are significantly inferior in the activity to the filtered ones, although in most cases they outperform the protonated precursors. After platinization, their activity proves to be 0.38% (HLT), 0.082% (HNT), 5.91% (HLT_3) and 3.70% (HNT_3). Despite the generally decent level of the photocatalytic performance achieved in aqueous methanol, the titanate nanosheets are somewhat behind the exfoliated niobates $HA_2Nb_3O_{10}$ (A = Ca, Sr) demonstrated maximum φ = 20.8% under the same conditions [103].

The rates of hydrogen evolution from pure water over the same photocatalysts inevitably turn out to be somewhat lower than from 1 mol.% methanol (Figure 9, Table 2) due to thermodynamic and kinetic limitations of the water splitting reaction [110–112]. However, several photocatalysts under study showed a very respectable activity level, allowing some progress to be made in this direction. In the case of HLT- and HNT-based samples, the photocatalytic performance, as usual, increases when going from the HCl-restacked NSs to filtered NSs and then to pristine ones. The latter outperform the protonated precursors in the hydrogen production rate by up to 50 times and allow reaching φ = 0.55%. Surprisingly, among the platinized HLT_3- and HNT_3-based photocatalysts the greatest activity in water is exhibited by the filtered NSs while the most active ones in a bare form are the pristine NSs as in all the other cases. The exact reason for this difference remains unclear. However, a much more important issue is the impressing hydrogen evolution activity demonstrated by HLT_3 filtered NSs/Pt in pure water (ω = 305 µmol/h, φ = 3.15%) without the addition of any sacrificial agents. For comparison, the maximum performance of the exfoliated niobates $HA_2Nb_3O_{10}$ (A = Ca, Sr) in water splitting was shown to be evidently lower (ω = 110 µmol/h, φ = 2.4%) [103].

The exfoliated and reassembled titanates HLT_3 and HNT_3 have also demonstrated their superiority over the well-known commercial photocatalyst TiO_2 P25 Degussa that was decorated with a 1% Pt cocatalyst and tested under the identical conditions. Particularly, TiO_2/Pt demonstrated maximum quantum efficiency of hydrogen generation of 8.96% and 2.03% in 1 mol.% methanol and pure water, respectively, while the titanates under consideration allowed achieving the values up to 14.2% and 3.15%.

Generally, analysis of the hydrogen evolution activity shown by the nanosheet-based photocatalysts (Figure 9, Table 2) allows identifying the following trends. First of all, most La-containing samples are seen to be superior in the activity to their Nd-containing counterparts. This difference is especially expressed between the platinized HLT- and HNT-based catalysts. After platinization, both pristine and reassembled HLT nanosheets are tens of times more active than corresponding HNT ones despite the similar chemical composition, bandgap energy and even smaller specific surface area (Table 1). The same difference was reported earlier for the organically modified photocatalysts based on HLT and HNT titanates [70]. One of the potential reasons for this may be associated with the presence of f-electrons in the Nd shell and resulting absorption in the visible spectrum region. Such absorption may be a factor responsible for lower activity of the Nd-containing photocatalysts due to a change in the electron configuration of excited Nd atoms as well as additional heating of the particles due to the absorption of visible radiation from the lamp. Besides this, HLT filtered NSs exhibit a higher photoluminescence lifetime than HNT filtered ones upon excitation in the intrinsic absorption region (Table 1), which may point to a lower charge carrier recombination rate in the former. This fact is consistent with the unequal photocatalytic performance of these samples, although it does not fully explain the strong difference in the platinization efficiency (k_{Pt} in Table 2) of HLT- and HNT-filtered NSs. Among the HLT_3- and HNT_3-based catalysts, a similar trend can also be revealed but it is much less pronounced. Additionally, the exfoliated n = 3 titanates significantly outperform in the hydrogen evolution activity the n = 1 ones, which was also observed earlier for their inorganic–organic derivatives [69,70]. This may be associated with better spatial separation of photogenerated electrons and holes in the triple-layer perovskite slabs than in the single-layer ones, although the photoluminescence lifetimes measured do not show crucial differences between the n = 3 and n = 1 titanates in question.

Finally, the most significant issue in the context of this study is a relationship between the form of the nanosheet-based photocatalyst used and its hydrogen evolution activity. As follows from the above, the latter typically decreases when going from the pristine NSs to filtered NSs and then to HCl-restacked ones. The slightly lower activity of the filtered NSs in comparison with that of the pristine ones proves to be quite expected since the filtration process inevitably leads to the particle aggregation and their initial morphology cannot be restored via repeated sonication. A more intriguing thing is the significantly enhanced activity of the filtered NSs as compared to that of the HCl-restacked ones despite the smaller specific surface of the former (Table 1). As already noted, the measured specific surface area characterizes dry samples. Meanwhile, the filtered NSs undergo ultrasound-assisted disaggregation in aqueous media much easier than their HCl-restacked counterparts and give smaller particle sizes in the final suspensions (Figure 7). This, apparently, provides a greater active surface of the filtered NSs in a redispersed form and, therefore, explains their improved performance. Furthermore, the photoluminescence lifetimes of the filtered NSs exceed those of the HCl-restacked ones (Table 1) indicating a lower intensity of the electron–hole recombination in the former, which should be favorable for their photocatalytic properties. Furthermore, the filtered NSs, unlike HCl-restacked ones, represent some sort of hybrid inorganic–organic materials due to the TBA^+ cations strongly embedded between the stacked layers. Taking into account the above, one of tetrabutylammonium's key roles may be that its cations prevent adjacent perovskite nanosheets from tightly adhering to each other and, therefore, facilitate their ultrasonic disaggregation and increase the active surface area. In addition, organic modification of the interlayer space of layered perovskite-like oxides was earlier reported to result in a drastic increase in the hydrogen evolution activity exceeding two orders of magnitude [67,69–73]. Although the reassembled nanosheets with the interlayer TBA^+ cations are not completely similar to the mentioned inorganic–organic compounds, it seems reasonable to assume that, in our case, the bound organics might have a beneficial effect on the photocatalytic activity too. For instance, it could hypothetically serve as an additional reducing agent facilitating the Pt cocatalyst deposition on the sample surface.

Stability of the nanosheet-based photocatalysts obtained was confirmed by the linear course of the hydrogen evolution kinetic curves (Figure 8) indicating preservation of the reaction rate throughout the measurement duration. Long-term stability of the most active HLT_3- and HNT_3-based photocatalysts under study—pristine NSs/Pt and filtered NSs/Pt—was also examined via performing several running cycles in aqueous methanol with a total duration of 12 h (Figure S9). It was found that the hydrogen evolution activity remains at a level of no less than 90% of its original value. Some of the photocatalysts were isolated from the reaction suspensions after photocatalytic measurements and analyzed by SEM (Figure S10). The final samples were found to represent loose aggregates of perovskite nanosheets with a noticeable number of voids between particles. In addition, all the photocatalytic experiments included monitoring the stability of the reaction suspensions towards sedimentation, which was evaluated by the ratio of volume photocatalyst concentrations at the beginning and at the ending of each measurement (c_2/c_1). As one can see from Table S1, in most cases the pristine NSs demonstrate noticeably greater stability than the protonated titanates as well as filtered and HCl-restacked NSs. The reassembled titanates, on the contrary, form less stable suspensions and are more susceptible to settling on the reactor walls despite the continuous stirring. However, this practically does not affect the hydrogen evolution activity, which follows from the linear course of most kinetic curves (Figures 8 and S4–S8).

The photocatalytic hydrogen generation from aqueous methanol is accompanied by a decrease in pH of the reaction medium, which is especially expressed in the case of highly active platinized samples (Table S1). This experimental fact may point to the partial methanol oxidation to formic acid. To consider this issue, the reaction solutions were sampled after 12 and 24 h of hydrogen generation over HLT_3 filtered NSs/Pt, filtered and analyzed by means of Raman spectroscopy (Figure S11). The spectra obtained clearly show a decrease in the intensity of methanol vibrational bands (for instance, C–O stretching at $\approx$1015 cm^{-1}) due to the lowering of its concentration in the solution. At the same time, several new bands appear to coincide with O–C–O ($\approx$700 cm^{-1}) and H–C–O ($\approx$1400 cm^{-1}) bending modes in a molecule of formic acid. However, another new band that could be related to C=O stretching ($\approx$1715 cm^{-1}) is strongly broadened and its maximum is slightly shifted to the high frequency range from the position expected for formic acid ($\approx$1695 cm^{-1}). Moreover, the spectra also show an expressed peak at $\approx$905 cm^{-1} that cannot be attributed to the acid. According to reference data, these Raman peaks coincide with the most intense bands in the spectrum of methyl formate (C–O and C=O stretching in the ester group at $\approx$1715 and $\approx$905 cm^{-1}, respectively). The H–C–O bending frequency

($\approx$1400 cm^{-1}) is active in the spectra of both formic acid and methyl formate while the O–C–O mode ($\approx$700 cm^{-1}) is observed only in that of the acid. Thus, it might be assumed that formic acid produced in the course of the methanol oxidation reacts with the excess of the latter under the photocatalytic experiment conditions giving methyl formate. Meanwhile, the Raman bands of both formic acid and methyl formate are seen to be relatively weak even after conversion of almost half of the methanol (Figure S11). This fact indirectly points to the probable existence of other channels of methanol transformations that are not obvious from the Raman spectra (for instance, complete oxidation to carbon dioxide and water with the liberation of the former from the solution). However, the assumptions made require verification in a more detailed study.

4. Conclusions

In this study, Ruddlesden–Popper titanates $HLnTiO_4$ and $H_2Ln_2Ti_3O_{10}$ (Ln = La, Nd) have been successfully exfoliated into nanosheets that, in turn, have been systematically investigated as hydrogen evolution photocatalysts. The nanosheet-based samples demonstrated by up to 88 times greater photocatalytic performance in comparison with the bulk precursors and, after surface decoration with Pt nanoparticles, provided apparent quantum efficiency of hydrogen production up to 14.2% in 1 mol.% aqueous methanol and 3.15% in pure water without any sacrificial agents. It was revealed that exfoliated titanates $H_2Ln_2Ti_3O_{10}$ noticeably outperform their counterparts $HLnTiO_4$ in the activity, and the La-containing samples are more active than Nd-containing ones. Furthermore, the form in which the nanosheets are used strongly affects the hydrogen production efficiency. In most cases, the latter decreases when going from the pristine nanosheets to filtered ones and then to those restacked by hydrochloric acid. The unequal activity of two types of the reassembled titanates follows from the differences in their physical–chemical characteristics being influenced by the reassembly approach chosen. Particularly, the filtered nanosheets represent in some sense hybrid inorganic–organic materials with tetrabutylammonium cations strongly embedded between the stacked layers. They demonstrate improved charge carrier lifetimes and better dispersibility in aqueous media, which provides smaller sizes of their suspended particles despite lower specific surface areas in a dry state. The nanosheets restacked by hydrochloric acid, on the contrary, are practically devoid of the residual organics and show poorer lifetimes of photogenerated electron–hole pairs. Although they possess higher specific surface in a dry form, they are less dispersible in aqueous media and give greater particle sizes in the suspensions. As a consequence, the filtered nanosheets demonstrate evidently higher hydrogen production rates than their counterparts precipitated by the acid. The similar behavior was observed earlier for the exfoliated Dion–Jacobson niobates $HA_2Nb_3O_{10}$ (A = Ca, Sr). Thus, the aforementioned difference between filtered and acid-restacked nanosheets represents a universal tendency rather than just a special case. Therefore, the precipitation by acids does not seem an optimal approach to the preparation of nanosheet-based photocatalysts of hydrogen production despite its wide use in the available literature.

Supplementary Materials: The following supporting information can be downloaded at https://www.mdpi.com/article/10.3390/solids6020016/s1. Figure S1: Emission spectrum of the DRT-125 lamp with photocatalyst absorption regions; Figure S2: TG curves of the protonated titanates and their reassembled nanosheets; Figure S3: Photoluminescence spectra (a, b) and decay graphs (c–h) for the protonated titanates HLT_3, HNT_3 and their reassembled nanosheets; Figure S4: Kinetic curves of photocatalytic hydrogen evolution from 1 mol.% aqueous methanol and water over bare and platinized protonated titanates HLT, HNT, HLT_3 and HNT_3; Figure S5: Kinetic curves of photocatalytic hydrogen evolution from water over bare and platinized HLT nanosheet-based photocatalysts; Figure S6: Kinetic curves of photocatalytic hydrogen evolution from 1 mol.% aqueous methanol and water over bare and platinized HNT nanosheet-based photocatalysts; Figure S7: Kinetic curves of photocatalytic hydrogen evolution from 1 mol.% aqueous methanol and water over bare and platinized HLT_3 nanosheet-based photocatalysts; Figure S8: Kinetic curves of photocatalytic hydrogen evolution from 1 mol.% aqueous methanol and water over bare and platinized HNT_3 nanosheet-based photocatalysts; Figure S9: Hydrogen generation rate from 1 mol.% aqueous methanol over platinized HLT_3 and HNT_3 nanosheet-based photocatalysts after several running cycles; Figure S10: SEM images of HLT_3 NSs/Pt and HNT_3 NSs/Pt isolated from the reaction suspensions after standard photocatalytic experiments in 1 mol.% aqueous methanol; Figure S11: Raman spectra of 5 mol.% aqueous methanol solutions before and after photocatalytic experiments of various durations with HLT_3 filtered NSs/Pt; Table S1: Data on pH (pH_1—before, pH_2—after the photocatalytic experiment) and sedimentation stability of the reaction suspensions (c_2/c_1—ratio of volume photocatalyst concentrations at the ending and at the beginning of the photocatalytic experiment); Information S1: Detailed procedure for preparing the precursors for exfoliation; Information S2: Detailed procedure for photocatalytic measurements; Information S3: Scheme and operating principle of the photocatalytic setting; Information S4: Determination of the lamp photon flux.

Author Contributions: Conceptualization, S.A.K. and O.I.S.; methodology, S.A.K., O.I.S. and I.A.R.; validation, O.I.S. and I.A.Z.; investigation, S.A.K. and I.A.M.; resources, O.I.S. and I.A.R.; data curation, O.I.S.; writing—original draft preparation, S.A.K.; writing—review and editing, S.A.K. and O.I.S.; visualization, S.A.K. and I.A.R.; supervision, O.I.S.; project administration, O.I.S.; funding acquisition, O.I.S. All authors have read and agreed to the published version of the manuscript.

Funding: This research and the APC were funded by the Russian Science Foundation, grant number 22-73-10110.

Data Availability Statement: The research data are available in the article body and Supplementary Materials.

Acknowledgments: This research was conducted using the equipment of the Saint Petersburg State University Research Park: Center for X-ray Diffraction Studies, Center for Optical and Laser Research, Center for Chemical Analysis and Materials Research, Center for Thermal Analysis and Calorimetry, Interdisciplinary Center for Nanotechnology, Center for Diagnostics of Functional Materials for Medicine, Pharmacology and Nanoelectronics, Center for Innovative Technologies of Composite Nanomaterials.

Conflicts of Interest: The authors declare no conflicts of interest.

References

1. Goodarzi, N.; Ashrafi-Peyman, Z.; Khani, E.; Moshfegh, A.Z. Recent Progress on Semiconductor Heterogeneous Photocatalysts in Clean Energy Production and Environmental Remediation. *Catalysts* **2023**, *13*, 1102. [CrossRef]
2. Sharma, S.; Kumar, R.; Raizada, P.; Ahamad, T.; Alshehri, S.M.; Nguyen, V.H.; Thakur, S.; Nguyen, C.C.; Kim, S.Y.; Le, Q.; et al. An Overview on Recent Progress in Photocatalytic Air Purification: Metal-Based and Metal-Free Photocatalysis. *Environ. Res.* **2022**, *214*, 113995. [CrossRef] [PubMed]
3. Lee, D.E.; Kim, M.K.; Danish, M.; Jo, W.K. State-of-the-Art Review on Photocatalysis for Efficient Wastewater Treatment: Attractive Approach in Photocatalyst Design and Parameters Affecting the Photocatalytic Degradation. *Catal. Commun.* **2023**, *183*, 106764. [CrossRef]
4. Fujishima, A.; Honda, K. Electrochemical Photolysis of Water at a Semiconductor Electrode. *Nature* **1972**, *238*, 37–38. [CrossRef] [PubMed]
5. Rozhkova, E.; Ariga, K. *From Molecules to Materials: Pathways to Artificial Photosynthesis*; Springer: Berlin/Heidelberg, Germany, 2015.
6. Ismail, A.A.; Bahnemann, D.W. Photochemical Splitting of Water for Hydrogen Production by Photocatalysis: A Review. *Sol. Energy Mater. Sol. Cells* **2014**, *128*, 85–101. [CrossRef]
7. Ahmad, H.; Kamarudin, S.K.; Minggu, L.J.; Kassim, M. Hydrogen from Photo-Catalytic Water Splitting Process: A Review. *Renew. Sustain. Energy Rev.* **2015**, *43*, 599–610. [CrossRef]
8. Takanabe, K. Photocatalytic Water Splitting: Quantitative Approaches toward Photocatalyst by Design. *ACS Catal.* **2017**, *7*, 8006–8022. [CrossRef]

9. Walter, M.G.; Warren, E.L.; McKone, J.R.; Boettcher, S.W.; Mi, Q.; Santori, E.A.; Lewis, N.S. Solar Water Splitting Cells. *Chem. Rev.* **2010**, *110*, 6446–6473. [CrossRef]
10. Kausar, F.; Varghese, A.; Pinheiro, D.; Devi, K.R.S. Recent Trends in Photocatalytic Water Splitting Using Titania Based Ternary Photocatalysts—A Review. *Int. J. Hydrogen Energy* **2022**, *47*, 22371–22402. [CrossRef]
11. Zhao, H.; Mao, Q.; Jian, L.; Dong, Y.; Zhu, Y. Photodeposition of Earth-Abundant Cocatalysts in Photocatalytic Water Splitting: Methods, Functions, and Mechanisms. *Chin. J. Catal.* **2022**, *43*, 1774–1804. [CrossRef]
12. Moridon, S.N.F.; Arifin, K.; Yunus, R.M.; Minggu, L.J.; Kassim, M.B. Photocatalytic Water Splitting Performance of TiO_2 Sensitized by Metal Chalcogenides: A Review. *Ceram. Int.* **2022**, *48*, 5892–5907. [CrossRef]
13. Li, R.; Li, C. Scalable Solar Water Splitting Using Particulate Photocatalysts. *Curr. Opin. Green Sustain. Chem.* **2022**, *33*, 100577. [CrossRef]
14. O'Neill, J.S.; Kearney, L.; Brandon, M.P.; Pryce, M.T. Design Components of Porphyrin-Based Photocatalytic Hydrogen Evolution Systems: A Review. *Coord. Chem. Rev.* **2022**, *467*, 214599. [CrossRef]
15. Bellardita, M.; García-López, E.I.; Marcì, G.; Palmisano, L. Photocatalytic Formation of H_2 and Value-Added Chemicals in Aqueous Glucose (Pt)-TiO_2 Suspension. *Int. J. Hydrogen Energy* **2016**, *41*, 5934–5947. [CrossRef]
16. Zhou, M.; Li, Y.; Peng, S.; Lu, G.; Li, S. Effect of Epimerization of D-Glucose on Photocatalytic Hydrogen Generation over Pt/TiO_2. *Catal. Commun.* **2012**, *18*, 21–25. [CrossRef]
17. Bahadori, E.; Ramis, G.; Zanardo, D.; Menegazzo, F.; Signoretto, M.; Gazzoli, D.; Pietrogiacomi, D.; Michele, A. Di Photoreforming of Glucose over CuO/TiO_2. *Catalysts* **2020**, *10*, 477. [CrossRef]
18. Bellardita, M.; García-López, E.I.; Marcì, G.; Nasillo, G.; Palmisano, L. Photocatalytic Solar Light H_2 Production by Aqueous Glucose Reforming. *Eur. J. Inorg. Chem.* **2018**, *2018*, 4522–4532. [CrossRef]
19. Iervolino, G.; Vaiano, V.; Murcia, J.J.; Rizzo, L.; Ventre, G.; Pepe, G.; Campiglia, P.; Hidalgo, M.C.; Navío, J.A.; Sannino, D. Photocatalytic Hydrogen Production from Degradation of Glucose over Fluorinated and Platinized TiO_2 Catalysts. *J. Catal.* **2016**, *339*, 47–56. [CrossRef]
20. Bello, M.O.; Prabhakar, S.; Abdus-salam, N.; Adekola, F.A.; Shobha, C.; Sesha, A.V.; Pal, U. Na-Y Zeolite Supported TiO_2/Pd Nanoparticles for Enhanced Photoredox Catalytic Properties and Green Hydrogen Generation. *Catal. Commun.* **2024**, *186*, 106817. [CrossRef]
21. Jiang, Z.; Ye, Z.; Shangguan, W. Recent Advances of Hydrogen Production through Particulate Semiconductor Photocatalytic Overall Water Splitting. *Front. Energy* **2022**, *16*, 49–63. [CrossRef]
22. Yao, Y.; Gao, X.; Meng, X. Recent Advances on Electrocatalytic and Photocatalytic Seawater Splitting for Hydrogen Evolution. *Int. J. Hydrogen Energy* **2021**, *46*, 9087–9100. [CrossRef]
23. Zhang, F.; Wang, Q. Redox-Mediated Electrocatalytic and Photocatalytic Hydrogen Production. *Curr. Opin. Electrochem.* **2022**, *35*, 101097. [CrossRef]
24. Sahani, S.; Malika Tripathi, K.; Il Lee, T.; Dubal, D.P.; Wong, C.P.; Chandra Sharma, Y.; Young Kim, T. Recent Advances in Photocatalytic Carbon-Based Materials for Enhanced Water Splitting under Visible-Light Irradiation. *Energy Convers. Manag.* **2022**, *252*, 115133. [CrossRef]
25. Chen, J.; Abazari, R.; Adegoke, K.A.; Maxakato, N.W.; Bello, O.S.; Tahir, M.; Tasleem, S.; Sanati, S.; Kirillov, A.M.; Zhou, Y. Metal–Organic Frameworks and Derived Materials as Photocatalysts for Water Splitting and Carbon Dioxide Reduction. *Coord. Chem. Rev.* **2022**, *469*, 214664. [CrossRef]
26. Jaryal, R.; Kumar, R.; Khullar, S. Mixed Metal-Metal Organic Frameworks (MM-MOFs) and Their Use as Efficient Photocatalysts for Hydrogen Evolution from Water Splitting Reactions. *Coord. Chem. Rev.* **2022**, *464*, 214542. [CrossRef]
27. Pattanayak, P.; Singh, P.; Bansal, N.K.; Paul, M.; Dixit, H.; Porwal, S.; Mishra, S.; Singh, T. Recent Progress in Perovskite Transition Metal Oxide-Based Photocatalyst and Photoelectrode Materials for Solar-Driven Water Splitting. *J. Environ. Chem. Eng.* **2022**, *10*, 108429. [CrossRef]
28. Liu, Y.; Yang, B.; He, H.; Yang, S.; Duan, X.; Wang, S. Bismuth-Based Complex Oxides for Photocatalytic Applications in Environmental Remediation and Water Splitting: A Review. *Sci. Total Environ.* **2022**, *804*, 150215. [CrossRef]
29. Subramanyam, P.; Meena, B.; Biju, V.; Misawa, H.; Challapalli, S. Emerging Materials for Plasmon-Assisted Photoelectrochemical Water Splitting. *J. Photochem. Photobiol. C Photochem. Rev.* **2022**, *51*, 100472. [CrossRef]
30. Weng, Y.C.; Li, Y.H.; Yuan, W.L.; Huang, L.W. Enhanced Photocatalytic Activity of Amphiphilic Single-Walled Carbon Nanohorn–$In_{0.2}Cd_{0.8}S$ Composites for Water Splitting. *Catal. Commun.* **2024**, *186*, 106818. [CrossRef]
31. Christoforidis, K.C.; Fornasiero, P. Photocatalytic Hydrogen Production: A Rift into the Future Energy Supply. *ChemCatChem* **2017**, *9*, 1523–1544. [CrossRef]
32. Puga, A.V. Photocatalytic Production of Hydrogen from Biomass-Derived Feedstocks. *Coord. Chem. Rev.* **2016**, *315*, 1–66. [CrossRef]
33. Liu, R.; Yoshida, H.; Fujita, S.; Arai, M. Photocatalytic Hydrogen Production from Glycerol and Water with NiO_x/TiO_2 Catalysts. *Appl. Catal. B Environ.* **2014**, *144*, 41–45. [CrossRef]

34. Taboada, E.; Angurell, I.; Llorca, J. Hydrogen Photoproduction from Bio-Derived Alcohols in an Optical Fiber Honeycomb Reactor Loaded with Au/TiO_2. *J. Photochem. Photobiol. A Chem.* **2014**, *281*, 35–39. [CrossRef]
35. Al-Azri, Z.H.N.; Chen, W.T.; Chan, A.; Jovic, V.; Ina, T.; Idriss, H.; Waterhouse, G.I.N. The Roles of Metal Co-Catalysts and Reaction Media in Photocatalytic Hydrogen Production: Performance Evaluation of M/TiO_2 Photocatalysts (M = Pd, Pt, Au) in Different Alcohol-Water Mixtures. *J. Catal.* **2015**, *329*, 355–367. [CrossRef]
36. Dosado, A.G.; Chen, W.T.; Chan, A.; Sun-Waterhouse, D.; Waterhouse, G.I.N. Novel Au/TiO_2 Photocatalysts for Hydrogen Production in Alcohol-Water Mixtures Based on Hydrogen Titanate Nanotube Precursors. *J. Catal.* **2015**, *330*, 238–254. [CrossRef]
37. Wang, X.; Dong, H.; Hu, Z.; Qi, Z.; Li, L. Fabrication of a Cu_2O/Au/TiO_2 Composite Film for Efficient Photocatalytic Hydrogen Production from Aqueous Solution of Methanol and Glucose. *Mater. Sci. Eng. B Solid-State Mater. Adv. Technol.* **2017**, *219*, 10–19. [CrossRef]
38. Li, C.; Wang, H.; Ming, J.; Liu, M.; Fang, P. Hydrogen Generation by Photocatalytic Reforming of Glucose with Heterostructured CdS/MoS_2 Composites under Visible Light Irradiation. *Int. J. Hydrogen Energy* **2017**, *42*, 16968–16978. [CrossRef]
39. Jaswal, R.; Shende, R.; Nan, W.; Shende, A. Photocatalytic Reforming of Pinewood (Pinus Ponderosa) Acid Hydrolysate for Hydrogen Generation. *Int. J. Hydrogen Energy* **2017**, *42*, 2839–2848. [CrossRef]
40. Irshad, M.; Ain, Q.; Zaman, M.; Aslam, M.Z.; Kousar, N.; Asim, M.; Rafique, M.; Siraj, K.; Tabish, A.N.; Usman, M.; et al. Photocatalysis and Perovskite Oxide-Based Materials: A Remedy for a Clean and Sustainable Future. *RSC Adv.* **2022**, *12*, 7009–7039. [CrossRef]
41. Schaak, R.E.; Mallouk, T.E. Perovskites by Design: A Toolbox of Solid-State Reactions. *Chem. Mater.* **2002**, *14*, 1455–1471. [CrossRef]
42. Uppuluri, R.; Sen Gupta, A.; Rosas, A.S.; Mallouk, T.E. Soft Chemistry of Ion-Exchangeable Layered Metal Oxides. *Chem. Soc. Rev.* **2018**, *47*, 2401–2430. [CrossRef] [PubMed]
43. Tani, S.; Komori, Y.; Hayashi, S.; Sugahara, Y. Local Environments and Dynamics of Hydrogen Atoms in Protonated Forms of Ion-Exchangeable Layered Perovskites Estimated by Solid-State ^{1} H NMR. *J. Solid. State Chem.* **2006**, *179*, 3357–3364. [CrossRef]
44. Nishimoto, S.; Matsuda, M.; Miyake, M. Novel Protonated and Hydrated Ruddlesden–Popper Phases, $H_xNa_{1-x}LaTiO_4{\cdot}yH_2O$, Formed by Ion-Exchange/Intercalation Reaction. *J. Solid. State Chem.* **2005**, *178*, 811–818. [CrossRef]
45. Nishimoto, S.; Matsuda, M.; Harjo, S.; Hoshikawa, A.; Kamiyama, T.; Ishigaki, T.; Miyake, M. Structure Determination of n=1 Ruddlesden–Popper Compound $HLaTiO_4$ by Powder Neutron Diffraction. *J. Eur. Ceram. Soc.* **2006**, *26*, 725–729. [CrossRef]
46. Jacobson, A.J.; Lewandowski, J.T.; Johnson, J.W. Ion Exchange of the Layered Perovskite $KCa_2Nb_3O_{10}$ by Protons. *J. Less Common. Met.* **1986**, *116*, 137–146. [CrossRef]
47. Jacobson, A.J.; Johnson, J.W.; Lewandowski, J.T. Interlayer Chemistry between Thick Transition-Metal Oxide Layers: Synthesis and Intercalation Reactions of $K[Ca_2Na_{n-3}Nb_nO_{3n+1}]$ ($3 \leq n \leq 7$). *Inorg. Chem.* **1985**, *24*, 3727–3729. [CrossRef]
48. Silyukov, O.I.; Kurnosenko, S.A.; Minich, I.A.; Rodionov, I.A.; Zvereva, I.A. Protonated Forms of Layered Perovskite-Like Titanate $NaNdTiO_4$: Neutron and X-Ray Diffraction Structural Analysis. *Solids* **2021**, *2*, 265–277. [CrossRef]
49. Zou, Z.; Ye, J.; Arakawa, H. Substitution Effects of In^{3+} by Fe^{3+} on Photocatalytic and Structural Properties of Bi_2InNbO_7 Photocatalysts. *J. Mol. Catal.* **2001**, *168*, 289–297. [CrossRef]
50. Reddy, V.; Hwang, D.; Lee, J. Effect of Zr Substitution for Ti in $KLaTiO_4$ for Photocatalytic Water Splitting. *Catal. Lett.* **2003**, *90*, 39–44. [CrossRef]
51. Kumar, V.; Govind; Uma, S. Investigation of Cation (Sn^{2+}) and Anion (N^{3-}) Substitution in Favor of Visible Light Photocatalytic Activity in the Layered Perovskite $K_2La_2Ti_3O_{10}$. *J. Hazard. Mater.* **2011**, *189*, 502–508. [CrossRef]
52. Zhou, Y.; Wen, T.; Guo, Y.; Yang, B.; Wang, Y. Controllable Doping of Nitrogen and Tetravalent Niobium Affords Yellow and Black Calcium Niobate Nanosheets for Enhanced Photocatalytic Hydrogen Evolution. *RSC Adv.* **2016**, *6*, 64930–64936. [CrossRef]
53. Kawashima, K.; Hojamberdiev, M.; Chen, S.; Yubuta, K.; Wagata, H.; Domen, K.; Teshima, K. Understanding the Effect of Partial N^{3-}-to-O^{2-} Substitution and H^+-to-K^+ Exchange on Photocatalytic Water Reduction Activity of Ruddlesden–Popper Layered Perovskite $KLaTiO_4$. *Mol. Catal.* **2017**, *432*, 250–258. [CrossRef]
54. Cui, W.; Qi, Y.; Liu, L.; Rana, D.; Hu, J.; Liang, Y. Synthesis of PbS–$K_2La_2Ti_3O_{10}$ Composite and Its Photocatalytic Activity for Hydrogen Production. *Prog. Nat. Sci. Mater. Int.* **2012**, *22*, 120–125. [CrossRef]
55. Cui, W.; Liu, L.; Ma, S.; Liang, Y.; Zhang, Z. CdS-Sensitized $K_2La_2Ti_3O_{10}$ Composite: A New Photocatalyst for Hydrogen Evolution under Visible Light Irradiation. *Catal. Today* **2013**, *207*, 44–49. [CrossRef]
56. Cui, W.; Guo, D.; Liu, L.; Hu, J.; Rana, D.; Liang, Y. Preparation of $ZnIn_2S_4$/$K_2La_2Ti_3O_{10}$ Composites and Their Photocatalytic H_2 Evolution from Aqueous Na_2S/Na_2SO_3 under Visible Light Irradiation. *Catal. Commun.* **2014**, *48*, 55–59. [CrossRef]
57. Saito, K.; Kozeni, M.; Sohmiya, M.; Komaguchi, K.; Ogawa, M.; Sugahara, Y.; Ide, Y. Unprecedentedly Enhanced Solar Photocatalytic Activity of a Layered Titanate Simply Integrated with TiO_2 Nanoparticles. *Phys. Chem. Chem. Phys.* **2016**, *18*, 30920–30925. [CrossRef]
58. Liu, Y.; Zhou, Y.; Lv, C.; Zhang, C.; Jin, X.; Meng, Q.; Chen, G. Construction of 2D-Composite $HCa_2Nb_3O_{10}$/$CaNb_2O_6$ Heterostructured Photocatalysts with Enhanced Hydrogen Production Performance. *New J. Chem.* **2018**, *42*, 681–687. [CrossRef]

59. Chen, X.; Shen, S.; Guo, L.; Mao, S.S. Semiconductor-Based Photocatalytic Hydrogen Generation. *Chem. Rev.* **2010**, *110*, 6503–6570. [CrossRef]
60. Zhang, L.; Wong, K.H.; Chen, Z.; Yu, J.C.; Zhao, J.; Hu, C.; Chan, C.Y.; Wong, P.K. AgBr-Ag-Bi_2WO_6 Nanojunction System: A Novel and Efficient Photocatalyst with Double Visible-Light Active Components. *Appl. Catal. A Gen.* **2009**, *363*, 221–229. [CrossRef]
61. Kim, H.G.; Jeong, E.D.; Borse, P.H.; Jeon, S.; Yong, K.; Lee, J.S.; Li, W.; Oh, S.H. Photocatalytic Ohmic Layered Nanocomposite for Efficient Utilization of Visible Light Photons. *Appl. Phys. Lett.* **2006**, *89*, 2012–2015. [CrossRef]
62. Kim, H.G.; Borse, P.H.; Choi, W.; Lee, J.S. Photocatalytic Nanodiodes for Visible-Light Photocatalysis. *Angew. Chem.* **2005**, *117*, 4661–4665. [CrossRef]
63. Zhang, L.; Wang, G.; Xiong, Z.; Tang, H.; Jiang, C. Fabrication of Flower-like Direct Z-Scheme β-Bi_2O_3/g-C_3N_4 photocatalyst with Enhanced Visible Light Photoactivity for Rhodamine B Degradation. *Appl. Surf. Sci.* **2018**, *436*, 162–171. [CrossRef]
64. Youngblood, W.J.; Anna Lee, S.H.; Maeda, K.; Mallouk, T.E. Visible Light Water Splitting Using Dye-Sensitized Oxide Semiconductors. *Acc. Chem. Res.* **2009**, *42*, 1966–1973. [CrossRef] [PubMed]
65. Machida, M.; Mitsuyama, T.; Ikeue, K.; Matsushima, S.; Arai, M. Photocatalytic Property and Electronic Structure of Triple-Layered Perovskite Tantalates, $MCa_2Ta_3O_{10}$ (M = Cs, Na, H, and $C_6H_{13}NH_3$). *J. Phys. Chem. B* **2005**, *109*, 7801–7806. [CrossRef]
66. Wang, Y.; Wang, C.; Wang, L.; Hao, Q.; Zhu, X.; Chen, X.; Tang, K. Preparation of Interlayer Surface Tailored Protonated Double-Layered Perovskite $H_2CaTa_2O_7$ with *n*-Alcohols, and Their Photocatalytic Activity. *RSC Adv.* **2014**, *4*, 4047–4054. [CrossRef]
67. Rodionov, I.A.; Maksimova, E.A.; Pozhidaev, A.Y.; Kurnosenko, S.A.; Silyukov, O.I.; Zvereva, I.A. Layered Titanate $H_2Nd_2Ti_3O_{10}$ Intercalated with *n*-Butylamine: A New Highly Efficient Hybrid Photocatalyst for Hydrogen Production from Aqueous Solutions of Alcohols. *Front. Chem.* **2019**, *7*, 863. [CrossRef]
68. Rodionov, I.A.; Gruzdeva, E.O.; Mazur, A.S.; Kurnosenko, S.A.; Silyukov, O.I.; Zvereva, I.A. Photocatalytic Hydrogen Generation from Aqueous Methanol Solution over *n*-Butylamine-Intercalated Layered Titanate $H_2La_2Ti_3O_{10}$: Activity and Stability of the Hybrid Photocatalyst. *Catalysts* **2022**, *12*, 1556. [CrossRef]
69. Kurnosenko, S.A.; Voytovich, V.V.; Silyukov, O.I.; Rodionov, I.A.; Kirichenko, S.O.; Minich, I.A.; Malygina, E.N.; Khramova, A.D.; Zvereva, I.A. Photocatalytic Activity of *n*-Alkylamine and *n*-Alkoxy Derivatives of Layered Perovskite-like Titanates $H_2Ln_2Ti_3O_{10}$ (Ln = La, Nd) in the Reaction of Hydrogen Production from an Aqueous Solution of Methanol. *Catalysts* **2021**, *11*, 1279. [CrossRef]
70. Kurnosenko, S.A.; Voytovich, V.V.; Silyukov, O.I.; Rodionov, I.A.; Zvereva, I.A. Photocatalytic Activity and Stability of Organically Modified Layered Perovskite-like Titanates $HLnTiO_4$ (Ln = La, Nd) in the Reaction of Hydrogen Evolution from Aqueous Methanol. *Catalysts* **2023**, *13*, 749. [CrossRef]
71. Kurnosenko, S.A.; Voytovich, V.V.; Silyukov, O.I.; Rodionov, I.A.; Zvereva, I.A. Photocatalytic Hydrogen Production from Aqueous Solutions of Glucose and Xylose over Layered Perovskite-like Oxides $HCa_2Nb_3O_{10}$, $H_2La_2Ti_3O_{10}$ and Their Inorganic-Organic Derivatives. *Nanomaterials* **2022**, *12*, 2717. [CrossRef]
72. Voytovich, V.V.; Kurnosenko, S.A.; Silyukov, O.I.; Rodionov, I.A.; Minich, I.A.; Zvereva, I.A. Study of *n*-Alkylamine Intercalated Layered Perovskite-like Niobates $HCa_2Nb_3O_{10}$ as Photocatalysts for Hydrogen Production from an Aqueous Solution of Methanol. *Front. Chem.* **2020**, *8*, 300. [CrossRef]
73. Voytovich, V.V.; Kurnosenko, S.A.; Silyukov, O.I.; Rodionov, I.A.; Bugrov, A.N.; Minich, I.A.; Malygina, E.N.; Zvereva, I.A. Synthesis of *n*-Alkoxy Derivatives of Layered Perovskite-like Niobate $HCa_2Nb_3O_{10}$ and Study of Their Photocatalytic Activity for Hydrogen Production from an Aqueous Solution of Methanol. *Catalysts* **2021**, *11*, 897. [CrossRef]
74. Maeda, K.; Mallouk, T.E. Two-Dimensional Metal Oxide Nanosheets as Building Blocks for Artificial Photosynthetic Assemblies. *Bull. Chem. Soc. Jpn.* **2018**, *92*, 38–54. [CrossRef]
75. Hu, Y.; Mao, L.; Guan, X.; Tucker, K.A.; Xie, H.; Wu, X.; Shi, J. Layered Perovskite Oxides and Their Derivative Nanosheets Adopting Different Modification Strategies towards Better Photocatalytic Performance of Water Splitting. *Renew. Sustain. Energy Rev.* **2020**, *119*, 109527. [CrossRef]
76. Ebina, Y.; Sasaki, T.; Harada, M.; Watanabe, M. Restacked Perovskite Nanosheets and Their Pt-Loaded Materials as Photocatalysts. *Chem. Mater.* **2002**, *1*, 4390–4395. [CrossRef]
77. Zheng, B.; Mao, L.; Shi, J.; Chen, Q.; Hu, Y.; Zhang, G.; Yao, J.; Lu, Y. Facile Layer-by-Layer Self-Assembly of 2D Perovskite Niobate and Layered Double Hydroxide Nanosheets for Enhanced Photocatalytic Oxygen Generation. *Int. J. Hydrogen Energy* **2021**, *46*, 34276–34286. [CrossRef]
78. Nicolosi, V.; Chhowalla, M.; Kanatzidis, M.G.; Strano, M.S.; Coleman, J.N. Liquid Exfoliation of Layered Materials. *Science* **2013**, *340*, 1226419. [CrossRef]
79. Yuan, H.; Nguyen, M.; Hammer, T.; Koster, G.; Rijnders, G.; Ten Elshof, J.E. Synthesis of $KCa_2Nb_3O_{10}$ Crystals with Varying Grain Sizes and Their Nanosheet Monolayer Films As Seed Layers for PiezoMEMS Applications. *ACS Appl. Mater. Interfaces* **2015**, *7*, 27473–27478. [CrossRef]

80. Xu, F.F.; Ebina, Y.; Bando, Y.; Sasaki, T. Structural Characterization of (TBA,H)$Ca_2Nb_3O_{10}$ Nanosheets Formed by Delamination of a Precursor-Layered Perovskite. *J. Phys. Chem. B* **2003**, *107*, 9638–9645. [CrossRef]
81. Xu, J.; Xia, B.; Wang, M.; Fan, Z.; Zhang, X.; Ma, J.; Liu, L.; Zhang, B.; Zhang, D.; Tong, Z. A Biosensor Consisting of $Ca_2Nb_3O_{10}^-$ Substrates and Functional Molecule Manganese Porphyrins (MnTMPyP) Utilized for the Determinations of Nitrite. *Funct. Mater. Lett.* **2018**, *11*, 1850053. [CrossRef]
82. Ohisa, S.; Hikichi, T.; Pu, Y.J.; Chiba, T.; Kido, J. Two-Dimensional $Ca_2Nb_3O_{10}$ Perovskite Nanosheets for Electron Injection Layers in Organic Light-Emitting Devices. *ACS Appl. Mater. Interfaces* **2018**, *10*, 27885–27893. [CrossRef] [PubMed]
83. Hojamberdiev, M.; Bekheet, M.F.; Zahedi, E.; Wagata, H.; Kamei, Y.; Yubuta, K.; Gurlo, A.; Matsushita, N.; Domen, K.; Teshima, K. New Dion-Jacobson Phase Three-Layer Perovskite $CsBa_2Ta_3O_{10}$ and Its Conversion to Nitrided $Ba_2Ta_3O_{10}$ Nanosheets via a Nitridation-Protonation-Intercalation-Exfoliation Route for Water Splitting. *Cryst. Growth Des.* **2016**, *16*, 2302–2308. [CrossRef]
84. Wang, T.H.; Henderson, C.N.; Draskovic, T.I.; Mallouk, T.E. Synthesis, Exfoliation, and Electronic/Protonic Conductivity of the Dion-Jacobson Phase Layer Perovskite $HLa_2TiTa_2O_{10}$. *Chem. Mater.* **2014**, *26*, 898–906. [CrossRef]
85. Sakaki, M.; Feng, Y.Q.; Kajiyoshi, K. Ultrasonic-Assisted Exfoliation of $Ca_2Nb_3O_{10}^-$ Nano-Sheets. *J. Solid. State Chem.* **2019**, *277*, 253–259. [CrossRef]
86. Oshima, T.; Nishioka, S.; Kikuchi, Y.; Hirai, S.; Yanagisawa, K.I.; Eguchi, M.; Miseki, Y.; Yokoi, T.; Yui, T.; Kimoto, K.; et al. An Artificial Z-Scheme Constructed from Dye-Sensitized Metal Oxide Nanosheets for Visible Light-Driven Overall Water Splitting. *J. Am. Chem. Soc.* **2020**, *142*, 8412–8420. [CrossRef]
87. Nishioka, S.; Hojo, K.; Xiao, L.; Gao, T.; Miseki, Y.; Yasuda, S.; Yokoi, T.; Sayama, K.; Mallouk, T.E.; Maeda, K. Surface-Modified, Dye-Sensitized Niobate Nanosheets Enabling an Efficient Solar-Driven Z-Scheme for Overall Water Splitting. *Sci. Adv.* **2022**, *8*, eadc9115. [CrossRef]
88. Yang, Y.; Xiong, J.; Song, Y.; Zou, J.; Wu, L. Preparation of Monolayer $HSr_2Nb_3O_{10}$ Nanosheets for Photocatalytic Hydrogen Evolution. *Dalt. Trans.* **2019**, *48*, 11136–11141. [CrossRef]
89. Maeda, K.; Mallouk, T.E. Comparison of Two- and Three-Layer Restacked Dion–Jacobson Phase Niobate Nanosheets as Catalysts for Photochemical Hydrogen Evolution. *J. Mater. Chem.* **2009**, *19*, 4813–4818. [CrossRef]
90. Shi, J.; Mao, L.; Cai, C.; Li, G.; Cheng, C.; Zheng, B.; Hu, Y.; Huang, Z.; Hu, X.; Żyła, G. One-Pot Fabrication of 2D/2D $HCa_2Nb_3O_{10}$/g-C_3N_4 Type II Heterojunctions towards Enhanced Photocatalytic H_2 Evolution under Visible-Light Irradiation. *Catal. Sci. Technol.* **2020**, *10*, 5896–5902. [CrossRef]
91. Luo, D.; Huang, Y.; Zhao, Y.; Fang, Y.; Li, Z.; Guo, Q.; Wei, Y.; Fan, L.; Wu, J. Visible-Light-Driven $HSr_2Nb_3O_{10}$/CdS Heterojunctions for High Hydrogen Evolution Activity. *Int. J. Hydrogen Energy* **2020**, *45*, 2896–2908. [CrossRef]
92. Li, D.; Zhou, C.; Liang, X.; Shi, X.; Song, Q.; Chen, M.; Jiang, D. Noble-Metal-Free Mo_2C Co-Catalsyt Modified Perovskite Oxide Nanosheet Photocatalysts with Enhanced Hydrogen Evolution Performance. *Colloids Surf. A Physicochem. Eng. Asp.* **2021**, *615*, 126252. [CrossRef]
93. Xie, Z.; Liang, X.; Jiang, D.; Chen, M. Noble-Metal-Free Co_xP Nanoparticles: Modified Perovskite Oxide Ultrathin Nanosheet Photocatalysts with Significantly Enhanced Photocatalytic Hydrogen Evolution Activity. *Nanotechnology* **2020**, *31*, 325401. [CrossRef] [PubMed]
94. Li, D.; Zhao, H.; Li, L.; Mao, B.; Chen, M.; Shen, H.; Shi, W.; Jiang, D.; Lei, Y. Graphene-Sensitized Perovskite Oxide Monolayer Nanosheets for Efficient Photocatalytic Reaction. *Adv. Funct. Mater.* **2018**, *28*, 1806284. [CrossRef]
95. Nishioka, S.; Oshima, T.; Hirai, S.; Saito, D.; Hojo, K.; Mallouk, T.E.; Maeda, K. Excited Carrier Dynamics in a Dye-Sensitized Niobate Nanosheet Photocatalyst for Visible-Light Hydrogen Evolution. *ACS Catal.* **2021**, *11*, 659–669. [CrossRef]
96. Maeda, K.; Sahara, G.; Eguchi, M.; Ishitani, O. Hybrids of a Ruthenium(II) Polypyridyl Complex and a Metal Oxide Nanosheet for Dye-Sensitized Hydrogen Evolution with Visible Light: Effects of the Energy Structure on Photocatalytic Activity. *ACS Catal.* **2015**, *5*, 1700–1707. [CrossRef]
97. Greene, W.N.; Roy, N. Photocatalytic Hydrogen Evolution from Hexaniobate Nanoscrolls and Calcium Niobate Nanosheets Sensitized by Ruthenium(II) Bipyridyl Complexes. *J. Phys. Chem. C* **2009**, *113*, 7962–7969. [CrossRef]
98. Ida, S.; Ogata, C.; Eguchi, M.; Youngblood, W.J.; Mallouk, T.E.; Matsumoto, Y. Photoluminescence of Perovskite Nanosheets Prepared by Exfoliation of Layered Oxides, $K_2Ln_2Ti_3O_{10}$, $KLnNb_2O_7$, and $RbLnTa_2O_7$ (Ln: Lanthanide Ion). *J. Am. Chem. Soc.* **2008**, *130*, 7052–7059. [CrossRef]
99. Schaak, R.E.; Mallouk, T.E. Prying Apart Ruddlesden-Popper Phases: Exfoliation into Sheets and Nanotubes for Assembly of Perovskite Thin Films. *Solid. State Ion.* **2000**, *12*, 3427–3434. [CrossRef]
100. Kawashima, K.; Hojamberdiev, M.; Wagata, H.; Yubuta, K.; Domen, K.; Teshima, K. Protonated Oxide, Nitrided, and Reoxidized $K_2La_2Ti_3O_{10}$ Crystals: Visible-Light-Induced Photocatalytic Water Oxidation and Fabrication of Their Nanosheets. *ACS Sustain. Chem. Eng.* **2017**, *5*, 232–240. [CrossRef]
101. Kurnosenko, S.A.; Silyukov, O.I.; Minich, I.A.; Zvereva, I.A. Exfoliation of Methylamine and *n*-Butylamine Derivatives of Layered Perovskite-like Oxides $HLnTiO_4$ and $H_2Ln_2Ti_3O_{10}$ (Ln = La, Nd) into Nanolayers. *Glas. Phys. Chem.* **2021**, *47*, 372–381. [CrossRef]

102. Kurnosenko, S.A.; Minich, I.A.; Silyukov, O.I.; Zvereva, I.A. Highly Efficient Liquid-Phase Exfoliation of Layered Perovskite-like Titanates $HLnTiO_4$ and $H_2Ln_2Ti_3O_{10}$ (Ln = La, Nd) into Nanosheets. *Nanomaterials* **2023**, *13*, 3052. [CrossRef] [PubMed]
103. Kurnosenko, S.A.; Voytovich, V.V.; Silyukov, O.I.; Rodionov, I.A.; Malygina, E.N.; Zvereva, I.A. Influence of $HB_2Nb_3O_{10}$-Based Nanosheet Photocatalysts (B = Ca, Sr) Preparation Method on Hydrogen Production Efficiency. *Catalysts* **2023**, *13*, 614. [CrossRef]
104. Ding, Y.; Luo, D.; Huang, Y.; Rong, B.; Chen, X.; Wei, Y.; Fan, L.; Wu, J. Microwave-Mechanochemistry-Assisted Synthesis of Z-Scheme $HSr_2Nb_3O_{10}/WO_3$ Heterojunctions for Improved Simulated Sunlight Driven Photocatalytic Activity. *J. Environ. Chem. Eng.* **2021**, *9*, 104624. [CrossRef]
105. Xiong, J.; Jing, K.; Zou, J.; Liang, S.; Wu, L. A Hybrid of $CdS/HCa_2Nb_3O_{10}$ Ultrathin Nanosheets for Promoting Photocatalytic Hydrogen Evolution. *Dalt. Trans.* **2017**, *46*, 13935–13942. [CrossRef]
106. Sun, Y.; Wen, B.; Jiang, D.; Li, D. CdS Nanoparticles Decorated $K^+Ca_2Nb_3O_{10}^-$ Nanosheets with Enhanced Photocatalytic Activity. *Mater. Lett.* **2018**, *229*, 236–239. [CrossRef]
107. Jiang, D.; Wang, T.; Xu, Q.; Li, D.; Meng, S.; Chen, M. Perovskite Oxide Ultrathin Nanosheets/g-C_3N_4 2D-2D Heterojunction Photocatalysts with Significantly Enhanced Photocatalytic Activity towards the Photodegradation of Tetracycline. *Appl. Catal. B Environ.* **2017**, *201*, 617–628. [CrossRef]
108. Ma, X.; Jiang, D.; Xiao, P.; Jin, Y.; Meng, S.; Chen, M. 2D/2D Heterojunctions of WO_3 Nanosheet/$K^+Ca_2Nb_3O_{10}^-$ Ultrathin Nanosheet with Improved Charge Separation Efficiency for Significantly Boosting Photocatalysis. *Catal. Sci. Technol.* **2017**, *7*, 3481–3491. [CrossRef]
109. Kurnosenko, S.A.; Voytovich, V.V.; Silyukov, O.I.; Minich, I.A.; Malygina, E.N.; Zvereva, I.A. Inorganic-Organic Derivatives of Layered Perovskite-like Titanates $HLnTiO_4$ (Ln = La, Nd) with *n*-Amines and *n*-Alcohols: Synthesis, Thermal, Vacuum and Hydrolytic Stability. *Ceram. Int.* **2022**, *48*, 7240–7252. [CrossRef]
110. Bie, C.; Wang, L.; Yu, J. Challenges for Photocatalytic Overall Water Splitting. *Chem* **2022**, *8*, 1567–1574. [CrossRef]
111. Gupta, A.; Likozar, B.; Jana, R.; Chanu, W.C.; Singh, M.K. A Review of Hydrogen Production Processes by Photocatalytic Water Splitting—From Atomistic Catalysis Design to Optimal Reactor Engineering. *Int. J. Hydrogen Energy* **2022**, *47*, 33282–33307. [CrossRef]
112. Hota, P.; Das, A.; Maiti, D.K. A Short Review on Generation of Green Fuel Hydrogen through Water Splitting. *Int. J. Hydrogen Energy* **2022**, *48*, 523–541. [CrossRef]